

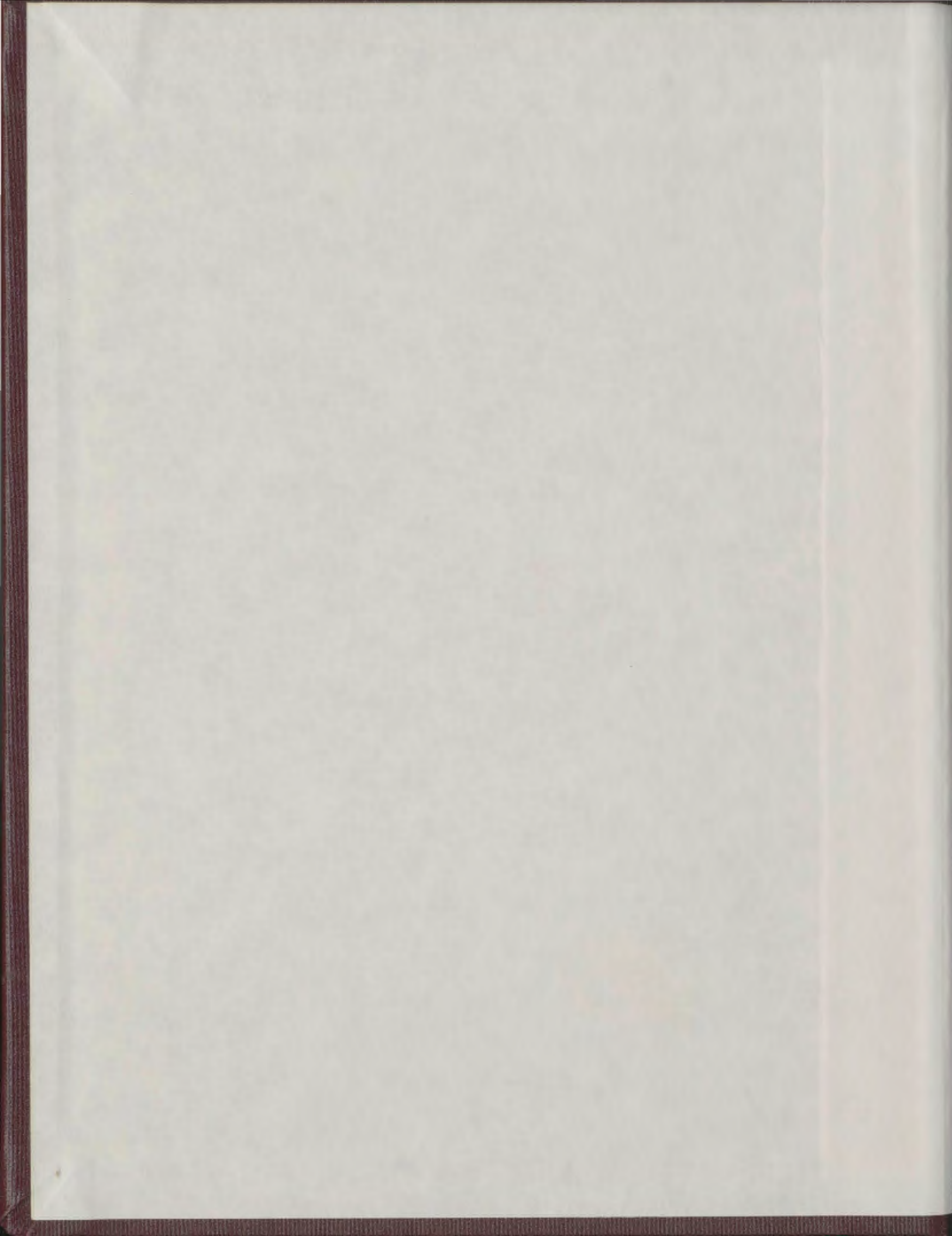
ANOMALOUS BEHAVIOUR IN  
THE VIBRATIONAL RAMAN  
SPECTRA OF N<sub>2</sub>, O<sub>2</sub>, AND CO  
UNDER NEAR-CRITICAL  
CONDITIONS

CENTRE FOR NEWFOUNDLAND STUDIES

**TOTAL OF 10 PAGES ONLY  
MAY BE XEROXED**

(Without Author's Permission)

NAUSHAD ALI



11153





ANOMALOUS BEHAVIOUR IN THE VIBRATIONAL RAMAN SPECTRA  
OF N<sub>2</sub>, O<sub>2</sub>, AND CO UNDER NEAR-CRITICAL CONDITIONS

by

Naushad Ali, M.Sc. (A.M.U.)



A Thesis submitted in partial fulfillment  
of the requirements for the degree of  
Master of Science

Department of Physics  
Memorial University of Newfoundland

July 1978

St. John's

Newfoundland

ABSTRACT

Experimental studies of the isothermal density dependence of frequency shift and line-width of the Raman Q-branches of N<sub>2</sub>, O<sub>2</sub> and CO gases have been done. Light (514.5nm Wavelength) from an Ar-ion laser was focused at the centre of a temperature controlled cell containing the sample, and scattering at 90° was analyzed and recorded by photon counting techniques using a piezoelectrically scanned Fabry-Perot interferometer, photo-multiplier tube and a data acquisition and stabilization system.

The isothermal Raman frequency shift and line-width (FWHM) data were collected over a density range of 10 Amagat to 450 Amagat (70 psi - 1000 psi) for a set of temperatures close to the critical temperature (T<sub>c</sub>) for each gas (N<sub>2</sub>, O<sub>2</sub> & CO). It was found that the density dependences of both the shift and width exhibited anomalous behavior under near-critical conditions. The anomaly reduced for temperatures away from the critical temperature, and was found to vanish completely in the case of frequency shift at T-T<sub>c</sub> ≥ 3K.

The observed effects are qualitatively interpreted in terms of 'local density' fluctuations associated with molecular cluster formation. It is assumed that cluster condensation occurs at a particular value of density ρ<sub>CC</sub>, characterized by a large and sudden change in the mean cluster life-time. It is interpreted that for densities ρ < ρ<sub>CC</sub>, the observed Raman spectrum is mainly due to unclustered molecules and for densities ρ > ρ<sub>CC</sub>, the observed Raman spectrum is dominantly due to molecular clusters. Finally, it is concluded that the Raman effect could be of great importance as a probe of density fluctuations in the critical region.

ACKNOWLEDGEMENTS

The author is greatly indebted to Dr. M. J. Clouter and Dr. H. Kiefte for their continual guidance and encouragement throughout the course of this work and in the preparation of the thesis. I wish to thank Mr. R. Guest who devoted much time to the reproduction of the figures suitable for presentation. My thanks are also due to Mrs. G. L. Kerri for typing the thesis.

The financial assistance of Memorial University of Newfoundland in the form of a graduate fellowship and teaching assistantship is gratefully acknowledged.

TABLE OF CONTENTS

	Page
ABSTRACT	i
ACKNOWLEDGEMENTS	ii
TABLE OF CONTENTS	iii
LIST OF TABLES	v
LIST OF FIGURES	vi
CHAPTER 1 INTRODUCTION	1
CHAPTER 2 THEORY	8
2.1 Frequency Shift due to the Isotropic Intermolecular Forces	9
(a) The linear coefficient, a	10
(b) The quadratic coefficient, b	12
2.2 Motional Narrowing	14
CHAPTER 3 APPARATUS AND EXPERIMENTAL TECHNIQUE	17
3.1 Laser	17
3.2 Interferometer	20
3.3 Photo-multiplier Tube and Detection System	22
3.4 Data Acquisition and Stabilization System	23
3.5 Scattering Cell and Temperature Control	25
3.6 Cryostat	31
CHAPTER 4 RESULTS AND DISCUSSION	35
4.1 Procedure	35
4.2 Data	40
4.3 Discussion	40

	Page
(a) Relative Raman shift, $\nu - \nu_0$	77
(b) Line-width (FWHM), $\Gamma$	91
REFERENCES	96
APPENDIX A	99

LIST OF TABLES

	Page
Table 4.1	List of critical constants $\rho_c$ , and $T_c$ and calculated value of $(\nu_Q - \bar{\nu}_Q)$ for $N_2$ , $O_2$ and CO. 41
Table 4.2	List of the relative Raman frequency shift and the Raman line-width data, at different densities, for $N_2$ at three different temperatures. 42
Table 4.3	List of the relative Raman frequency shift and the Raman line-width data, at different densities, for $O_2$ at three different temperatures. 48
Table 4.4	List of the relative Raman frequency shift and the Raman line-width data, at different densities, for CO at four different temperatures. 55

LIST OF FIGURES

	Page	
Fig. 1.1	A resolved spectrum of the Raman Q-branch for dilute gaseous nitrogen at 77K.	4
Fig. 1.2	The Raman vibration-rotation band for N <sub>2</sub> which shows resolved O and S branches but an unresolved Q-branch.	4
Fig. 1.3	A resolved Raman Q-branch spectrum for H <sub>2</sub> at a density of 200 Amagat.	4
Fig. 3.1	Block diagram of the overall experimental set up.	19
Fig. 3.2	The scattering cell (vertical section).	27
Fig. 3.3	Block diagram for temperature control.	29
Fig. 3.4	The Cryostat.	33
Fig. 4.1	Shows a typical Raman Q-branch spectra for two different densities.	38
Fig. 4.2	Plots of relative Raman shift vs. density at different temperatures for N <sub>2</sub> .	64
Fig. 4.3	Plots of relative Raman shift vs. density at different temperatures for O <sub>2</sub> .	66

	Page
Fig. 4.4	Plots of relative Raman shift vs. density at different temperatures for CO. 68
Fig. 4.5	Plots of the full width at half maximum of the Raman Q-branch vs. density at different temperatures for N <sub>2</sub> . 70
Fig. 4.6	Plots of full width at half maximum of the Raman Q-branch vs. density at different temperatures for O <sub>2</sub> . 72
Fig. 4.7	Plots of full width at half maximum of the Raman Q-branch vs. density at different temperatures for CO. 74
Fig. 4.8	a) Plots of relative Raman shift vs. density at temperatures closest to T <sub>c</sub> (taken in this experiment) for N <sub>2</sub> , O <sub>2</sub> & CO, and b) corresponding plots for line-width. 76
Fig. 4.9	Showing the variations in the density distribution of unclustered molecules and clustered molecules with bulk density. 83
Fig. 4.10	Showing the Raman spectrum due to unclustered and clustered molecules and how this gives rise to the anomaly in $\nu - \nu_0$ near the critical region. 86

	Page
Fig. 4.11 Shows the occurrence of the anomaly given by the equations (4.8) and (4.9).	90

## CHAPTER 1

INTRODUCTION

The study of intermolecular forces by spectroscopic methods has been a fruitful field for many years. Such investigations when carried out with compressed gases, where the density and temperature can be easily and independently varied, are of special interest. There are of course a great variety of spectroscopic methods which can be used; these can be classified in a general way as emission, absorption and scattering procedures.

This thesis is concerned primarily with the density dependent effects of intermolecular forces upon the vibrational Raman spectra of simple gases. The gases chosen for this particular study were  $N_2$ ,  $O_2$  and  $CO$ .

As is well known, Raman scattering (1, 2) arises in gases as a result of the change of the polarizability tensor, caused by either rotation or vibration of the molecule. The anisotropic part of the polarizability tensor is responsible for the rotational and rotation-vibrational Raman scattering while variations in the isotropic part cause vibrational Raman scattering. The isotropic Raman scattering is highly polarized and occurs in the purely vibrational transitions (Q-branch) of the rotation-vibration Raman band of a totally symmetric vibration mode.

The selection rules (1, 2) ( $\Delta v = +1$ ,  $\Delta J = 0, \pm 2$ ) for the Raman spectrum of a vibrational transition allows for three branches namely, S-branch ( $\Delta J = 2$ ), O-branch ( $\Delta J = -2$ ) and Q-branch ( $\Delta J = 0$ ). The S and O branches are very much weaker since their lines are not superimposed. They form a series somewhat similar to the R and P

branches of the infrared bands except that the line separations (2) are about twice as large. A Raman vibration-rotation band for  $N_2$  is represented in Fig. (1.2), which shows resolved O and S branches but an unresolved Q-branch.

A Raman Q-branch is a series of closely spaced lines corresponding to the complete (populated) set of rotational states of the molecule. For the  $0 \rightarrow 1$  vibrational transition the difference between the rotation constants  $B_0$  and  $B_1$ , responsible for the separation between the Q-lines of a free molecule is very small; consequently all the lines of the Q-branch are very close. Fig. (1.1) shows a theoretically calculated spectrum of the Q-branch for dilute gaseous nitrogen at 77K. When the molecule is subjected to collisions in a compressed gas the individual lines of the branch broaden; however, when they overlap completely, as they do for most molecules at relatively low pressure, the phenomenon of "frequency degeneracy" (to be explained in chap. 2) occurs and the broadening ceases (3). It is for this reason that the Q-branch of  $N_2$ ,  $O_2$  and CO in the course of this work is observed as one unresolved band over all pressures used. The only molecules for which the Q-branches are readily resolved into individual lines upto fairly high pressures are  $H_2$ ,  $D_2$  and HD. A well resolved Raman Q-branch spectrum for  $H_2$  is shown in Fig. (1.3) at a density of 200 Amagat.

Since the effect of vibrational perturbation is superimposed on the Raman Q-branch, it is, in principle, an ideal one to study the action of intermolecular forces on molecular vibrations. The isotropic Q-lines are broadened and shifted in frequency due to molecular collisions. The theoretical investigation of collision broadening and shifting of the Raman spectra was done by Van Kranendonk and co-workers (3-6) using the so-called impact collision

FIGURE 1.1

A resolved theoretical spectrum of the Raman Q-branch for dilute gaseous nitrogen at 77K.

(Reprinted from Ref. (21)).

FIGURE 1.2

The Raman Vibration-rotation band for  $N_2$ , which shows resolved O and S branches but unresolved Q-branch.

(Reprinted from J. Opt. Soc. Am., 58, 311 (1968)).

FIGURE 1.3

A resolved Raman Q-branch spectrum for  $H_2$  at a density of 200 Amagat.

(Reprinted from Ref. (10)).

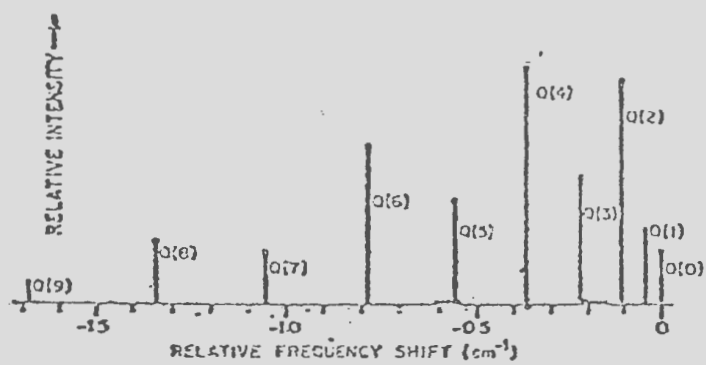


Fig. 1.1

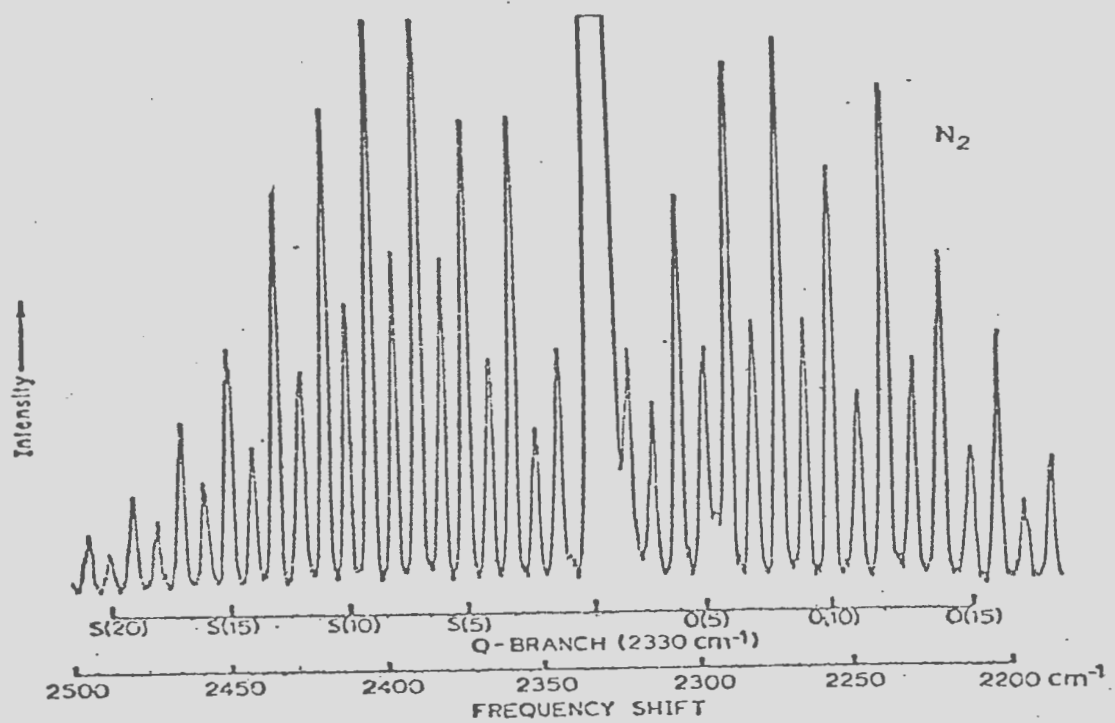


Fig. 1.2

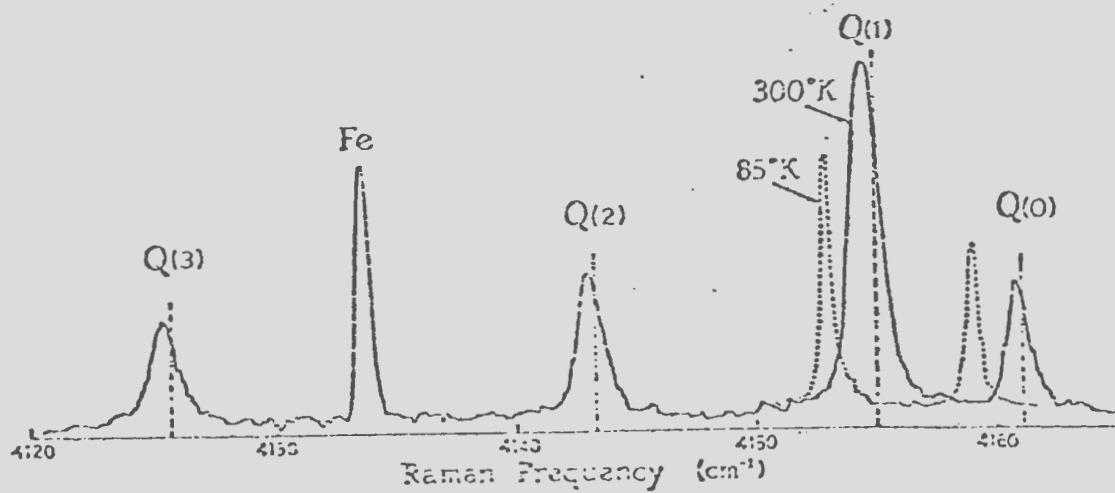


Fig. 1.3

approximation. The theory showed to a first approximation that the shifts in the Q-branch are produced only by perturbations of the vibrational motions of the molecules. Gray and Van Kranendonk (6) have shown that the anisotropic forces which broaden the vibrational lines do not contribute to the shifting. A somewhat different approach was proposed by Gordon (7, 8) but explicit calculations were not performed. Extensive experimental study has also been done. The work of the molecular physics group at the University of Toronto is of particular interest (9-17).

The Raman frequency shift measurements of the Q-lines of the hydrogen molecule has been well studied by May et al. (9, 10). These results were interpreted on the basis of a statistical model, with the basic assumption that the shifts are due entirely to vibrational perturbations. Their model shows that a systematic shift in the phase of the vibrational motion which leads to a shift in the vibrational frequency is caused by the isotropic intermolecular forces. Experimental results on the Raman frequency shift for  $H_2$ ,  $N_2$  and HD molecules (9-17) have been interpreted quite well by this model.

With respect to the vibrational Raman spectra in particular, there is another effect due to collisions which is the optical analogue of the motional narrowing in NMR (18). This effect was first observed by May (19) for CO and later by Varghese (12) for  $N_2$ . It was shown by Stryland et al. (20) that the width of the Q-branch of  $N_2$  decreases with increasing pressure. The band profile was found to be highly asymmetrical at low pressures, while very nearly symmetrical at high pressures. Observations of Scotto (21) and Clements and Stoicheff (22) have also shown that the band-width is further reduced in the liquid state and is much narrower than one

would expect from the splitting that arises from vibration-rotation interactions.

A partial explanation of the effect was given by Fiutak & Van Kranendonk (3), who refer to it as a "frequency degeneracy" phenomenon. The first theoretical explanation of the "motional narrowing" of the Raman Q-branch was given by Alekseyev & Sobelman (23, 24). They have determined the density dependence of Q-branch profile from independently broadened components at low densities, to overlapping, and then to narrowing of the band at high densities. Very recently Temkin & Burshtein (25) have also given a theoretical treatment of motional narrowing which is in agreement with the similar work of Brueck (26).

Experimentally, motional narrowing has been observed by May et al. (27), Wang & Wright (28) for  $N_2$  and CO molecules, by LeDuff (29) for  $N_2$  dissolved in  $SF_6$ , by LeDuff & Holzer (30) and by Altmann et al. (31) for  $H_2$ ,  $D_2$ , HF and  $N_2$  molecules dissolved in inert liquids. A qualitative agreement has been found between the theory and the experimental results. It has been quantitatively analyzed by May and co-workers (14-16) for compressed HD where the Q-branch components are well resolved over a wide range of densities. A theoretical calculation for Q-branch of HD has been presented recently by Bonamy et al. (43). Recent observations by Clouter and co-workers (32-33) for pure liquid  $N_2$ ,  $O_2$  and CO as well as the theoretical work of Brueck (26) indicate that motional narrowing may be the dominant effect over most of the liquid range. However, at the highest liquid densities, near the triple point, a different broadening mechanism comes into play. This effect which is referred to as "vibrational dephasing" has been investigated

in some detail by Laubereau and co-workers (34-36), but since it is not particularly relevant to the present work no further elaboration will be given. A more detailed resume of the theory associated with the vibrational frequency shift and motional narrowing is presented in Chapter 2. Chapter 3 gives a detailed description of the apparatus and the experimental techniques used. In Chapter 4 new data for the Raman Q-branch near the critical point of  $N_2$ ,  $O_2$  and CO molecules has been presented.

The main result of this work is the observation of previously unreported anomalies in the density dependence of both the frequency shift and width of the Q-branches under these (near-critical) conditions. A similar anomaly in intensity of the  $\nu_1$  band of  $CO_2$  in pressure induced absorption has been reported by Mannik and Stryland (37). A qualitative interpretation of the anomaly given in Chapter 4 indicates that such measurements may be of great value as a probe of the critical phenomenon.

## CHAPTER 2

THEORY

Since Raman scattering (1, 2) arises from the polarizability of a molecule one can see in a semi-classical way how collisions influence the spectrum. The polarizability tensor can be decomposed into a spherically symmetric component and an anisotropic component. The anisotropic component is a function of the phase of rotation and of the orientation of the angular momentum of the molecule. Thus either rotationally inelastic collisions or collisions which change the orientation of the angular momentum (or phase of rotation of a molecule) will broaden and shift the rotational Raman lines. Similarly, vibrationally inelastic collisions or collisions which shift the phase of the vibrational motion will broaden and shift the vibrational Raman lines.

There is also an indirect effect due to the rotation-vibration interaction which leads to the motional narrowing phenomenon. Molecules with different quantum number  $J$  will have slightly different vibrational frequencies, and rotationally inelastic collisions will cause the molecules to hop from one vibrational frequency (in the same vibrational level, due to very long  $1 \rightarrow 0$  relaxation time) to another. As the collision frequency increases the individual components of the Q-branch start overlapping, and in the region where the rotation-vibration interaction is comparable to the collision frequency the overlapping is complete and motional narrowing starts. In the following two sections, the Raman frequency shift and motional narrowing are dealt with separately.

## 2.1 Frequency Shift due to the Isotropic Intermolecular Forces

In a practical sense the perturbation of the vibrational frequencies of molecules is the most important of the spectral effects of the intermolecular forces. May *et al.* (9, 10) and Welsh *et al.* (11) have measured the frequency shift of the individual Q-branch components of compressed hydrogen molecules. Their interpretation was based on the principle that the frequency shifts associated with isotropic Raman scattering arise entirely from perturbations of the vibrational motion by isotropic interactions. It has in fact been shown by Gray & Van Kranendonk (6) that the anisotropic forces do not contribute to the shifting.

It was determined that the observed shift of a given Q-branch component (e.g. of H<sub>2</sub>) could be expressed in a virial type expansion in powers of the density (9, 10, 38),

$$\nu(J)_\rho - \nu(J) = a_J \rho + b_J \rho^2 + \dots \quad (2.1)$$

where,  $\nu(J)$  is the Raman frequency of a free molecule in rotational state J,  $a_J$  and  $b_J$  are J-dependent and temperature dependent constants. The co-efficient  $a_J$  has been found to be of the form,

$$a_J = a_i + a_c (m_J/m)$$

where,  $a_i$  and  $a_c$  are constants and  $m_J/m$  is the relative population of the initial rotational state J. The first term in equation (2.1) arises from binary interactions (9, 10), whereas the second term gives the contribution due to triple interactions which includes the contributions from the non-additive intermolecular forces (38, 39).

(a) The Linear Coefficient,  $a$ 

The coefficient  $a$  that describes the frequency shift due to binary interactions can be determined by assuming that the molecule is an anharmonic oscillator with an internuclear potential of the form;

$$U = f(r-r_e)^2 + g(r-r_e)^3 + j(r-r_e)^4 + \dots \quad (2.2)$$

The isotropic intermolecular potential of a pair of molecules 1 and 2 distant  $R_{12}$  apart can be written as,

$$\begin{aligned} V_{12}(R_{12}) = & V_{12}^e + (\partial V_{12}/\partial r_1)_e (r_1 - r_e) + (1/2)(\partial^2 V_{12}/\partial r_1^2)_e (r_1 - r_e)^2 \\ & + \dots + (\partial^2 V_{12}/\partial r_1 \partial r_2)_e (r_1 - r_e)(r_2 - r_e) \\ & + \dots + (\partial V_{12}/\partial r_2)_e (r_2 - r_e) + \dots \end{aligned} \quad (2.3)$$

where  $r_1$  and  $r_2$  are internuclear distances of the two molecules. In the calculation of the shift due to the isotropic forces, for binary interactions (apart from a 'coupling' effect to be discussed later) one can write for the potential energy of the perturbed molecule 1 with the help of equations (2.2) and (2.3):

$$\begin{aligned} U_1 = & f(r_1 - r_e)^2 + g(r_1 - r_e)^3 + j(r_1 - r_e)^4 + V_1'(r_1 - r_e) \\ & + (V_1''/2)(r_1 - r_e)^2 + \dots \end{aligned} \quad (2.4)$$

where,  $V_1' = \delta V_{12}/\delta r_1$ , etc.

The perturbation of the frequency of a Q-transition of molecule 1 by the second molecule due to isotropic intermolecular force is found to be

$$\Delta v_i = C_1 V_1' + C_2 V_1'' \quad (2.5)$$

where,  $C_1$  and  $C_2$  can be calculated from the known constants of the free molecule. Expressing the intermolecular potential in the Lennard-Jones form

$$V_{12} = A/R_{12}^{12} - B/R_{12}^6,$$

and differentiating  $V$  with respect to  $r_1$  one gets after substituting in equation (2.5),

$$\Delta v_i = (C_1 A_1' + C_2 A_1'')/R_{12}^{12} - (C_1 B_1' + C_2 B_1'')/R_{12}^6 \quad (2.6a)$$

or one can write

$$\Delta v_i = K_{\text{rep}}/R_{12}^{12} - K_{\text{att}}/R_{12}^6 \quad (2.6)$$

Thus  $\Delta v_i$  can be represented by the difference of two terms due to the repulsive and attractive forces and characterized by the parameters,  $K_{\text{rep}}$  and  $K_{\text{att}}$ .

The mean value of the total shift is obtained by summing the  $\Delta v_i$  over all perturbing molecules, multiplying the result by the molecular distribution function and integrating over all configuration space. This amounts to weighting equation (2.6) with the pair correlation function  $g(R_{12})$  and integrating over the variable  $R_{12}$ . An important assumption is made here that  $g(R_{12})$  can be expanded as a power series in the density that takes the form,

$$g(R_{12}) = g_0(R_{12}) + L\rho g_1(R_{12}) + L^2\rho^2 g_2(R_{12}) + \dots \quad (2.7)$$

After going through the procedure mentioned above one finds that  $a_i$  can be expressed as

$$a_i = K_{\text{rep}} I_1 - K_{\text{att}} I_2 \quad (2.8)$$

where,  $I_1$  and  $I_2$  are temperature dependent integrals given by,

$$I = L^2 \int R_{12}^{-q} \exp(-V(R_{12})/kT) \{ \exp(-V(R_{13})/kT) - 1 \} \\ \cdot \{ \exp(-V(R_{23})/kT) - 1 \} 4\pi R_{12}^2 dR_{12} dx_{13} dy_{13} dz_{13}, \quad (2.9)$$

with  $q=12$  and  $q=6$  for  $I_1$  and  $I_2$ , respectively.

For the calculation of the small 'coupling' term  $a_c$ , the potential energy used is;

$$U_{12} = f(r_1 - r_e)^2 + f(r_2 - r_e)^2 + (V''_{12}) (r_1 - r_e) (r_2 - r_e) + \dots \quad (2.10)$$

If the L-J potential is assumed for the interaction as was done for  $a_i$ , after applying the same statistical procedure as that for  $a_i$ , the mean shift due to coupling can be obtained as

$$\Delta v_c = (\omega_e/8f) \{ A''_{12} I_1 - B''_{12} I_2 \} \quad (m_J/m)$$

and 
$$a_c = (\omega_e/8f) \{ A''_{12} I_1 - B''_{12} I_2 \}$$

where,  $I_1$  and  $I_2$  are the same temperature dependent integrals as above.

(b) The quadratic coefficient,  $b$

The coefficient  $b$  describes the contribution to the shift from the triple interactions including the non-additive contribution and can be expressed as,

$$b = L^2 \int \Delta v(R_{12}) f_2^{(1)}(R_{12}) 4\pi R_{12}^2 dR_{12} + L^2 \int \int \{ \Delta v(R_1 R_2 R_3) - \Delta v(R_{12}) \\ - \Delta v(R_{13}) \} f_3^{(0)}(R_1 R_2 R_3) 16\pi^2 R_{12}^2 R_{13}^2 dR_{12} dR_{13} \quad (2.11)$$

where,  $L$  is Loschmidt's number, and the quantities  $\Delta v(R_1 R_2 R_3)$  and  $\Delta v(R_{12}) = \Delta v(R_1 R_2)$ , denote the vibrational frequency shift in a cluster of three and two molecules respectively. The function  $f_h^{(k)}(R_1 \dots R_h)$  is given by

$$y_h = \sum_{k=0}^{\infty} f_h^{(k)} (\rho L)^{h+k}$$

where,  $y_h$  is the configurational probability density; for  $h=2$  it is the same as the pair distribution function  $g(R_{12})$  mentioned above. The first term in the expression for  $b$  in equation (2.11) is due to the density dependence of the pair distribution function. The second term gives the contribution from the non-additive part of the shift in a cluster of three molecules.

The non-additive intermolecular potential,  $V_{na}(R_1 R_2 R_3)$  in a triple interaction is defined by

$$V(R_1 R_2 R_3) = V(R_1 R_2) + V(R_1 R_3) + V(R_2 R_3) - V_{na}(R_1 R_2 R_3)$$

As a model the theoretical expression taken for  $V_{na}$  is (40)

$$V_{na}(R_1 R_2 R_3) = \lambda h(R_1 R_2 R_3)$$

where  $\lambda = (3/2) (E_1 + E_2 + E_3) E_1 E_2 E_3 \alpha_1 \alpha_2 \alpha_3 / (E_1 + E_2) (E_2 + E_3) (E_3 + E_1)$

and  $h(R_1 R_2 R_3) = (3 \cos \theta_1 \cos \theta_2 \cos \theta_3 + 1) / (R_{12} R_{13} R_{23})^3$

In the above expressions,  $E_i$  and  $\alpha_i$  denote the ionization energy and mean polarizability of molecule,  $i$  and  $\theta_1$ ,  $\theta_2$  and  $\theta_3$  are the internal angles of the triangle formed by the three molecules.

Representing the additive intermolecular potential by a L-J model, one finds that

$$b = K_{\text{rep}}(I_3 + I_5) - K_{\text{att}}(I_4 - I_6) + K_{\text{na}} I_7$$

where,  $K_{\text{rep}}$  and  $K_{\text{att}}$  are the same as for  $a_j$  and  $K_{\text{na}} = C_1 \ell' + C_2 \ell''$ , while  $C_1$  and  $C_2$  have the same meaning as it is in the case of  $a_j$  and the dash denotes differentiation with respect to the internuclear distance in the central molecule.  $I_3 \dots I_7$  are temperature dependent integrals similar to  $I_1$  and  $I_2$  (10,39).

It is worth noting that in the present work, the linear term is by far the most important. For interest sake, the magnitudes of  $a_j$  and  $b_j$  for  $\text{H}_2$  at 85K are  $-9.76 \times 10^{-3} \text{ cm}^{-1}/\text{Amagat}$  and  $6.28 \times 10^6 \text{ cm}^{-1}/\text{Amagat}$  respectively, for  $J=1$  (10). The repulsive part of  $a_j$  is found to be strongly temperature dependent while the attractive part remains practically constant.

## 2.2 Motional Narrowing

It was Alekseyev and Sobelman (23,24) who first gave the theoretical explanation of motional narrowing treating the collisions between the molecules as binary and instantaneous with a simple two level model. Very recently Temkin & Burshtein (25) have developed a theoretical treatment of the motional narrowing of the Raman Q-branch in the strong-collision approximation.

When  $J' - J$  transitions occur because of inelastic rotational collisions, a change in the free molecule Q-transition frequency takes place. If the collisions are strong enough, then the prob-

---

Note: Section 2.1(b) has been outlined only in brief since it is not necessary for subsequent analysis.

ability of changing the frequency coincides with equilibrium Boltzmann distribution  $\phi(J)$ , given by

$$\phi(J) = \beta(2J+1) \exp \{-\beta J(J+1)\}$$

where,  $\beta = \hbar^2/2IkT$

$T$ , is the temperature and  $I$  is the moment of inertia of the molecule. The spectrum can be given by

$$G(\nu) = (1/\pi) \operatorname{Re} \int_0^{\infty} dQ(t) \exp(-i\nu(t+2\hbar/2kT)) dt = F(\nu) \exp(\hbar\nu/2kT)$$

where,  $dQ(t)$  is the correlation function of the polarizability tensor, and  $F(\nu)$  was found to be,

$$F(\nu) = (dQ(0)/\pi\bar{\nu}_Q) \operatorname{Im} \{ (\exp(-Z)) E_i(Z) / 1 + i\gamma (\exp(-Z)) E_i(Z) \}$$

where,  $\bar{\nu}_Q = \int_0^{\infty} \nu_Q \phi(J) dJ = \alpha_e T / (\hbar^2/2Ik)$

$$Z = \nu/\bar{\nu}_Q - i\gamma, \text{ and } \gamma = 1/\bar{\nu}_Q \tau_J,$$

and  $\tau_J$  is the relaxation time of the rotational angular momentum and  $\nu_Q$  is the frequency of the individual Q-branch components in the free molecule limit, given by  $\nu_Q = \alpha_e J(J+1)$ .

Now consider the two limiting cases of densities namely the very low density case ( $\gamma \rightarrow 0$ ) and the high density case ( $\gamma \gg 1$ ). In the low density limit  $F(\nu)$  reduces to the intensity distribution of a free classical rotator. While in the high density limit the half width of the isotropic band is given by

$$\Gamma = (\bar{\nu}_Q)^2 \tau_J$$

and the peak frequency of the band shifts from  $\nu_Q$  by an amount  $(\nu_Q - \bar{\nu}_Q)$ , where  $\nu_Q$  is the peak vibrational frequency of the Q-band for the free molecule. Considering the case of gases

$$\tau_J = (\rho\sigma_J v)^{-1}$$

where,  $v$  = average thermal velocity

$\sigma_J$  = cross-section for the scattering with change of rotational state

and  $\rho$  = gas density.

The full-width at half maximum (FWHM),  $\Gamma$ , is given by

$$\Gamma = 2(\rho\sigma_J v)^{-1} \{(\alpha_e/B_e)(kT/h)\}^2.$$

Hence, we see that the width of the isotropic band decreases inversely as the density increases. This is what is called the "motional narrowing" effect. It has been observed for gaseous  $N_2$ , CO and HD (13-17, 27, 28) and for liquid  $N_2$ ,  $O_2$  and CO (21, 32, 33).

Apart from motional narrowing, at very high densities the band may show some pure vibrational broadening. It has been reported for liquid  $O_2$  and  $N_2$  (32). At very high densities (e.g. liquid) where motional narrowing is complete the Raman line-width may be due to the "vibrational dephasing" as claimed by Laubereau & co-workers (34-36) for liquid  $N_2$ . However, it is the motional narrowing mechanism which is of greatest importance in the present case; therefore, no further elaboration of vibrational dephasing will be given.

## CHAPTER 3

APPARATUS AND EXPERIMENTAL TECHNIQUE

The overall arrangement of the apparatus used in this research is shown schematically in Fig. (3.1). Briefly, light from a single mode Ar-ion laser was focused at the centre of a temperature controlled cell containing the sample. The Raman scattered light at 90 degrees was analyzed by a piezoelectrically scanned Fabry-Perot interferometer (Burleigh Model RC-10). Photon counting techniques were used, with cooled ITT FW 130 photomultiplier tube (PMT) as the basic detector followed by an amplifier/discriminator (Princeton Applied Research Model SSR 1120) and a Fabry-Perot Data Acquisition and Stabilization System (Burleigh Model DAS-1). The apparatus and experimental techniques used will be described in some more detail under following headings:

1. Laser
2. Inteferometer
3. Photomultiplier Tube and Detection System
4. Data Acquisition and Stabilization System
5. Scattering Cell and Temperature Control
6. Cryostat

### 3.1 Laser

The incident light source used for the Raman line-width and frequency shift measurements, was an Ar-ion laser (Model 165-08 Spectra Physics). Basically, it consists of a high current

FIGURE 3.1

Block diagram of the overall experimental set-up.

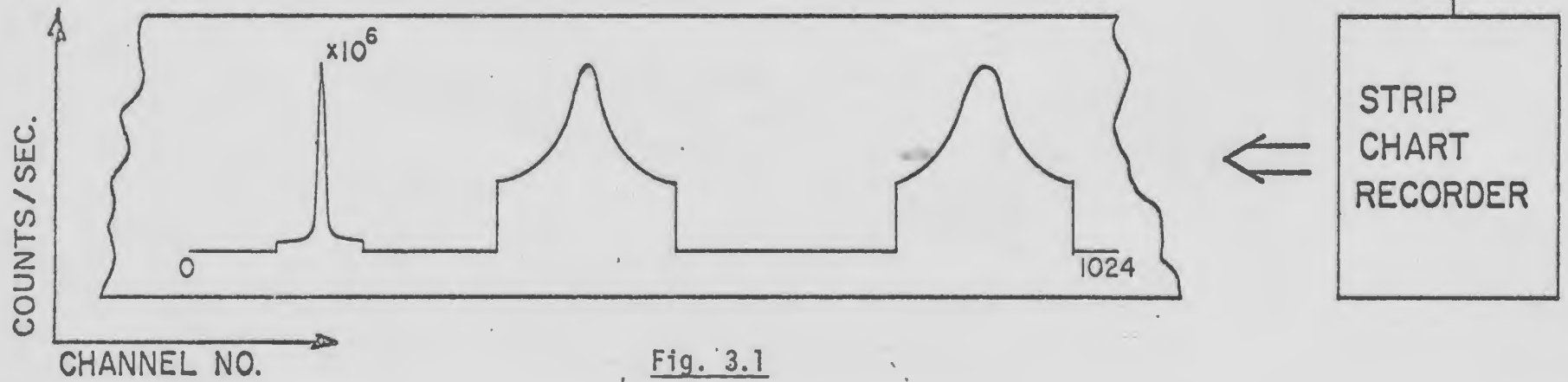
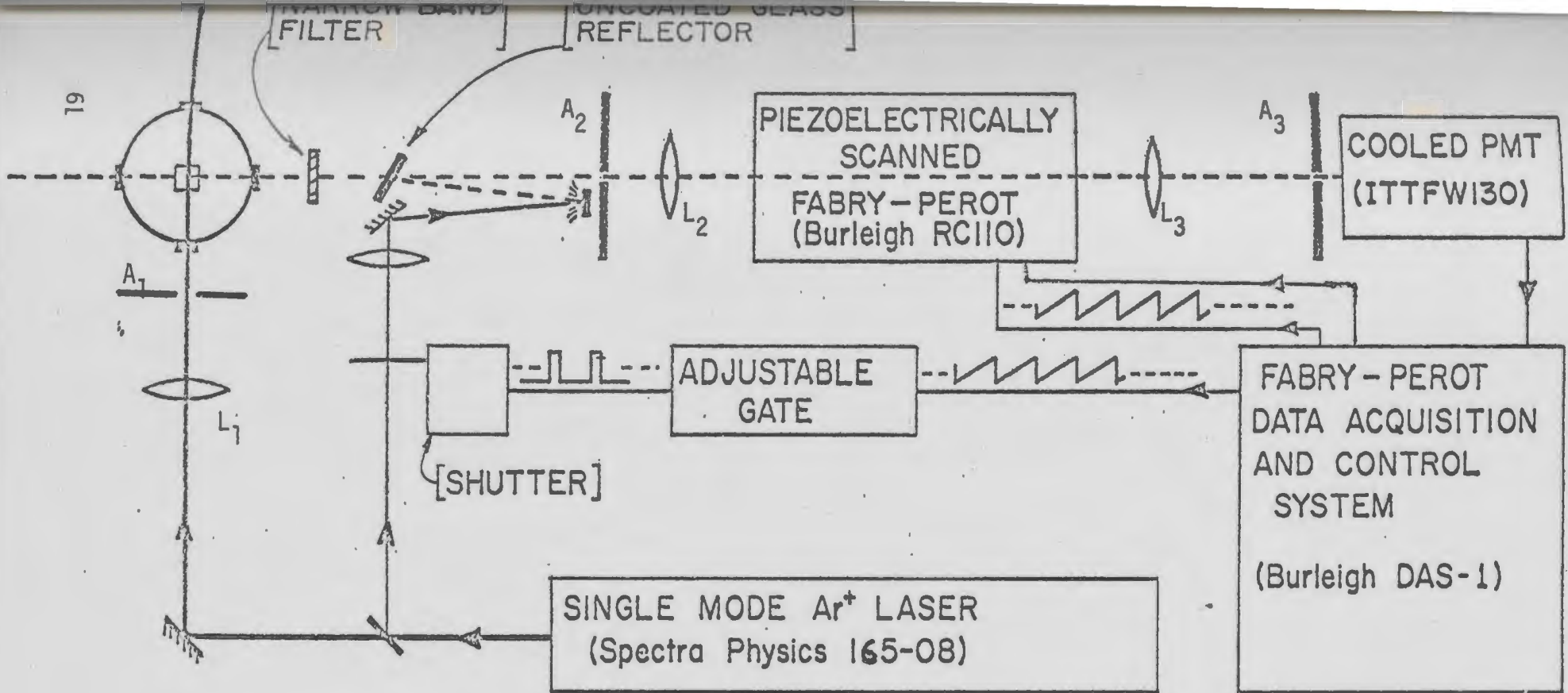


Fig. 3.1

gas discharge tube, excited with a direct current of about 25A and placed in an optical cavity of length 1.18 m. The principle laser emission was in the blue-green region of the visible spectrum. By the use of an intracavity prism one particular laser line at 514.5 nm was selected out of several individual lines, and was used throughout this research. The laser action of this line was restricted to one mode by using a temperature controlled intercavity etalon assembly (Model 589, Spectra Physics). The laser was found to be very stable and "mode-hopping" was absent for many hours of operation. The average width of the laser line due to high frequency "jitter" was found to be about  $\pm 5$  MHz.

The laser beam, always polarized perpendicular to the (horizontal) scattering plane, was focused at the centre of the sample cell by a lens ( $L_1$ ) of focal length 29.4 cm, through an aperture ( $A_1$ ). The Raman scattered light at 90 degrees was passed through a filter of about 10 nm band-width and was then collected by a second lens ( $L_2$ ) of focal length 50 cm, through an aperture ( $A_2$ ) and then directed into a Fabry-Perot interferometer for centre spot scanning.

### 3.2 Interferometer

The Fabry-Pérot (FP) interferometer, basically, consists of two partially transmitting mirrors held parallel to each other in an invar structure. If the FP cavity is illuminated by a beam of monochromatic light, it will transmit the beam when the condition for constructive interference

$$2nd \cos\theta = m\lambda$$

$$(3.1)$$

is satisfied.

$n$  is the refractive index of the medium between the two surfaces,

$d$  is the mirror spacing,

$\theta$  is angle between the transmitted beam and the normal to the surfaces,

$m$  is the order of interference,

and  $\lambda$  is the wavelength of the transmitted light.

Since the light transmitted along the optical axis (i.e.  $\theta=0^\circ$ ) was studied, therefore equation (3.1) reduces to,

$$m\lambda = 2d, \quad (n = 1, \text{ for air}).$$

By varying the spacing ( $d$ ) the order number and transmitted wavelength corresponding to  $\theta = 0^\circ$  are changed. Scanning is accomplished in moving one mirror with respect to the other by applying a highly linear sawtooth sweep voltage to the three piezoelectric elements (PZT's), supporting one of the mirrors at  $120^\circ$  spacings about its circumference. To a good approximation, the mirror separation ( $d$ ) varies linearly with the voltage applied to the PZT's. Alignment of the mirrors to  $\lambda/250$  parallelism is achieved first by differential screw adjustments and then by means of applying independent adjustment biases to each of the PZT's. The later operation was performed by the use of the Data Acquisition and Stabilization System (to be described later).

The main characteristics of the Fabry-Perot interferometer are its Spectral Free Range (SFR), and its Finesse ( $F$ ). The SFR, defined as the separation (in frequency or wavelength units) between two consecutive maxima, is given by

$$\text{SFR} = C/2nd \quad (\text{in Hz})$$

where, C is the velocity of light in vacuum. In these experiments several different SFR's were used by changing the mirror spacing. The instrumental width defined as the line-width (full width at half maximum) of a monochromatic light, is given by;

$$\Delta\nu = \text{SFR}/F$$

where, F is finesse. Consequently, we see that the finesse is the fundamental measure of the interferometer's resolving power.

The finesse is determined and limited, mainly by (1) mirror reflectivity of less than unity, (2) lack of parallelism and flatness of the mirror surfaces and (3) diffraction losses due to finite aperture of the interferometer. Contributions (1) and (2) are usually dominant. In this experiment  $\lambda/200$ , 2-inch plates with 98% reflectivity were used such that contribution (1) and (2) are approximately equal and the total finesse is given by  $F^{-2} = \sum_i F_i^{-2}$  ( $F_i$ 's are the individual contributions). An overall finesse of  $F \approx 60-70$  was attained throughout these experiments. Further detailed description of the F-P interferometer can be found in the M.Sc thesis of I.E. Morgan (41).

### 2.3 Photomultiplier Tube and Detection System

The light passing through the Fabry-Perot interferometer was focused with a lens ( $L_3$ ) of focal length 78.3 cm onto a pinhole ( $A_3$ ) placed in front of a photon detector. The detector used was a sensitive, low dark count, photomultiplier tube (PMT)

(ITT FW 130, Electro Optical Products Div. ITT). The low dark count was mainly due to the small photo-cathode area (0.25 cm diameter). The tube was mounted in a thermoelectrically cooled, RF - shielded chamber (Model TE 104 RF, Products for Research). Consequently, controlling the temperature of the cathode to  $(-20 \pm 0.5)^{\circ}\text{C}$  further reduced the dark count to a value of about 1 count per second.

A lens of focal length 7 cm was installed in the front end of the RF chamber to focus the light, coming through the pinhole ( $A_3$ ), on the small cathode area. The signal from the phototube was amplified and pulse-shaped by an amplifier/discriminator (AD) (Model SSR 1120, Princeton Applied Research) which was placed close to the phototube to prevent the attenuation of weak signal and stray pick-up in the leads. The amplified signal from the AD was fed to the scalar of the DAS-1 system in the form of 1 volt pulses (each pulse corresponding to a detected photon).

### 3.4 Data Acquisition and Stabilization System

Basically, the DAS-1 (Burleigh Instruments Inc.) provides for a digital voltage sweep to scan the Fabry-Perot, automatic correction for thermal drift of the mirror spacing and frequency drift of the source, automatic finesse optimization of the Fabry-Perot, and a 1024 channel multichannel analyzer (MCA) to accumulate and manipulate the data. The instrument was designed for recording weak spectra and hence repetitive scanning of the Fabry-Perot interferometer is employed.

A ramp voltage supplied by the DAS-1 is used to drive the

PZT's of the Fabry-Perot through a high voltage amplifier. Each of the 1024 channels are sequentially addressed in synchronism with the scanning of the FP by the same ramp voltage. Each time a photo-pulse arrives a count is added to the memory channel corresponding to that section of the ramp voltage. The number of the incremented channel corresponds directly to the ramp voltage. As a result, the frequency spectrum of the scattered light accumulates in the memory of the DAS-1. Data acquisition is prohibited by logic circuitry during the fly-back portion of the ramp wave-form.

The axial drift stabilization portion of the DAS-1 eliminates the effect of long term frequency drift of the laser or axial drift of the interferometer cavity. It does this by centering a given line in the spectrum (in this case a laser component) in a sensing window consisting of a group of channels bracketing the peak of the line. After each sweep the instrument performs a comparison of the number of counts in each half of the window and any tendency of the chosen line to drift from the center of the window is nullified by the application of a correction bias to the PZT's of the FP interferometer. The magnitude of the correction bias can be adjusted by a factor of 16:1 in steps of 2x depending on the ramp repetition rate and the drift rate.

Finesse optimization (i.e. correction for misalignment of the interferometer cavity) is done by a similar technique as axial drift stabilization. Counts in the finesse window centered on the reference line are accumulated on each sweep. On every second sweep, a smallest voltage is applied to the PZT elements to tilt

the mirrors first in  $\phi$  direction and then in  $\theta$  direction. The logic circuit compares the counts and tries to maximize the number of counts by applying proper correction voltage.

The DAS-1 also incorporates a provision (Segmented Time Base) that allows the ramp to slow down for specified regions of the spectrum; speed ratios and the extent of the fast and slow regions are manually adjustable. Since the ramp addresses both the FP and the channel numbers, the display remains linear in frequency.

As the count rate was very low in these experiments, the above provision was used to reduce the time for spectra recording. The spectrum is simultaneously accumulated in the DAS-1 memory and is continuously displayed on a CRT. An intensified spot called "Bug" can be positioned to address any channel of the memory. The alphanumeric portion of the CRT displays the Bug channel number, the total number of counts in that channel, and the full scale of the CRT display. Background subtraction is another useful feature of the DAS-1. The output from the DAS-1 is fed to a strip chart recorder to record the spectrum permanently.

### 3.5 Cell and Temperature Control

The scattering cell used in these experiments (Fig. 3.2) was specially designed by Clouter et al.(42) to withstand the large temperature and pressure variations. The cell was of miniaturized design for mainly three reasons: (1) the effect of differential thermal expansion between the different materials involved would thereby be considerably reduced; (2) in view of the type of the cryostat and the cooling method employed, small sample dimensions

FIGURE 3.2

## The Scattering Cell (vertical section)

- I Gas inlet tube.
  - P Brass post (one of two).
  - F Free gap.
  - Q Quartz window.
  - G Epoxy resin cement
  - Cu Copper foil.
  - In Indium solder.
  - Wp BeCu window plate.
  - O Indium O-ring.
  - T<sub>1</sub> Platinum thermometer well.
  - T<sub>2</sub> Secondary thermometer well (not used in present experiments).
- The control thermometer (GaAs not shown) was located on the front face of the cell between the posts P.

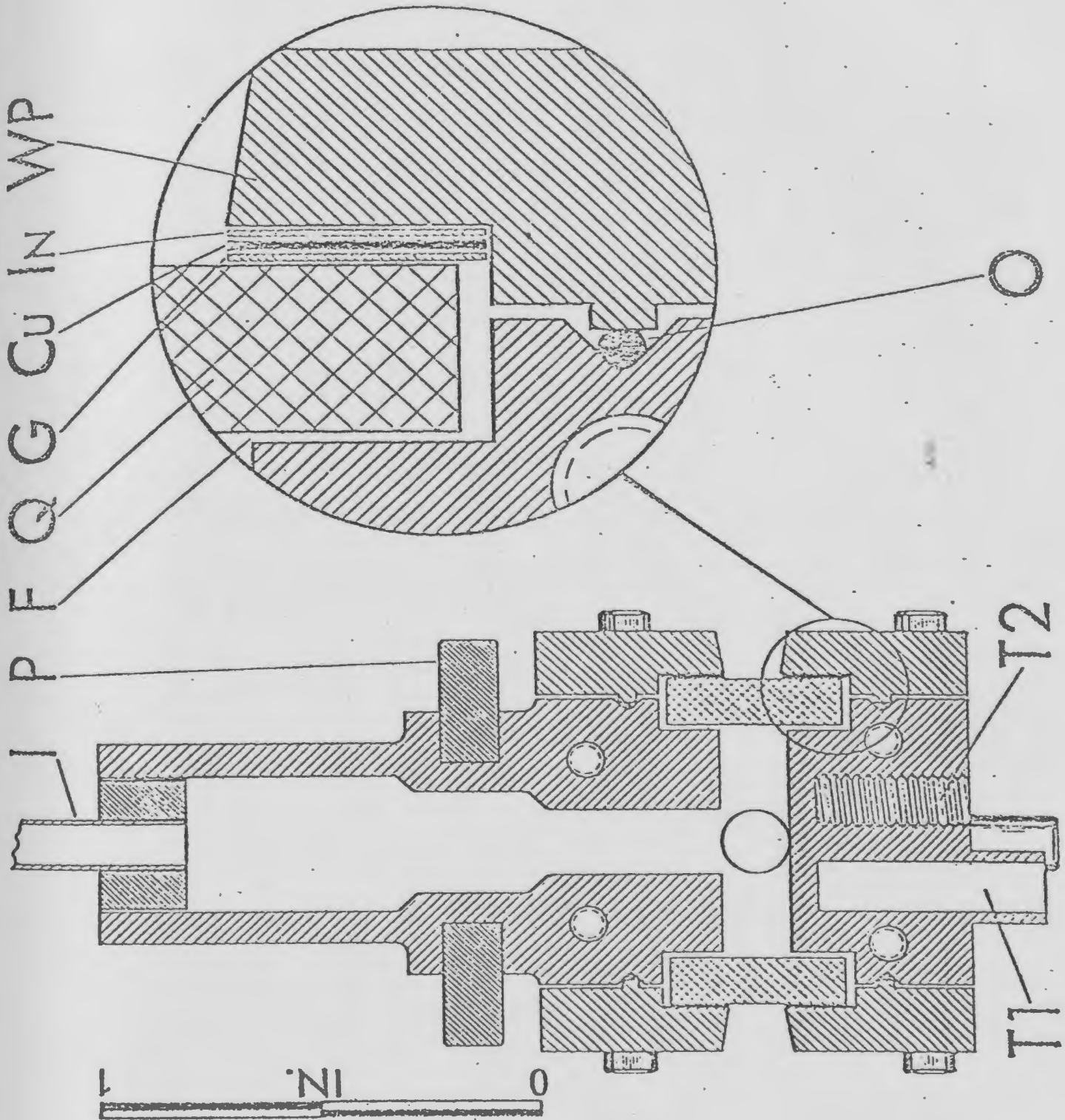
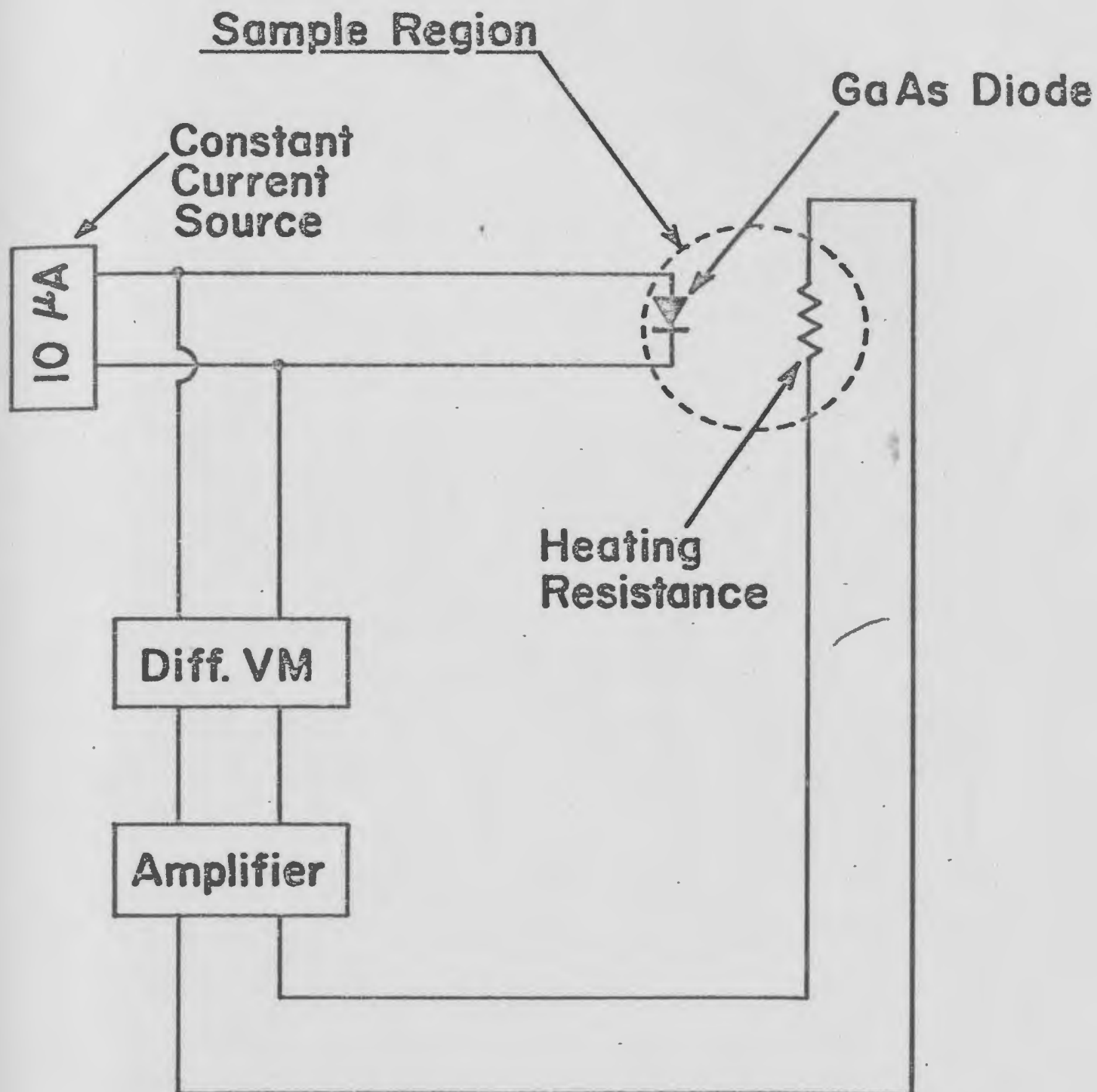


Fig. 3.2

would serve to minimize the thermal gradients which could otherwise contribute significant errors in the temperature measurements; and (3) the working space within the cryostat was somewhat small. The cell was machined entirely from a 5 cm length of 2.5 cm diameter BeCu alloy. The scattering volume was located at the intersection of three mutually perpendicular holes; two horizontal, one vertical. The horizontal holes were of 3.2 mm diameter. The four openings in the horizontal holes were then sealed by quartz windows (Q) (10 mm diameter and 3.2 mm thickness). The manner in which a reliable seal was obtained between each of the quartz window and the cell body is shown in the Fig. (3.2). A ring of 0.025mm copper foil was soldered with pure indium to the inside surface of each of four BeCu window plates (WP) and the windows were then attached with epoxy resin cement to the copper foil. Each of the window plates were sealed against the cell body via an indium O-ring (O) and four steel screws (#2-56); the mating surfaces were pretinned with indium.

The mechanical flexibility of the indium/copper foil/epoxy sandwich proved sufficient to relieve any stress due to differential thermal expansion between the BeCu and the quartz. In addition, the formation of this seal on a separate window plate instead of directly against the cell body resulted in the internal pressure assisting rather than inhibiting the seal. Also, the cell was surrounded by the cryostat vacuum so that when the cell was evacuated there was no back pressure which would tend to break the window seal.



**Block Diagram for Temperature Control System:**

Fig. 3.3

The laser beam passed straight through the cell via two windows; the light scattered at 90 degrees through a third window was analyzed by the FP and the fourth window was used for visual observation of the sample and for alignment purposes. The gas inlet tube I (3.2 mm diameter stainless steel, 0.15 mm thick wall) was hard soldered into the top of the cell providing communication with the gas handling system.

Thermal contact between the cell and the cryostat was made by two copper braids which were soft soldered to the posts (P) (180 degrees apart) and extended upwards up to about 5 cm at which point they were attached to a heat sink at the bottom end of a heat exchange column of the cryostat. Two electrical heaters of resistance 25 ohms each were wound on the posts and connected in series; these were used in conjunction with a GaAs thermometer to control the cell temperature (see Fig. 3.3).

The GaAs diffused junction thermometer is a diode whose forward voltage changes with temperature when a constant current is passed through it. In these experiments the constant current was  $10\mu\text{A}$ . The signal was fed to a differential voltmeter, and was compared with highly stable internal set point voltage; the difference (i.e. the error signal) was fed to an amplifier and the amplified signal was used to regulate the amount of current flowing through the heaters wound in series around the posts. This automatic control of temperature was stable to within about 0.02K for a few hours.

A platinum resistance thermometer,  $T_1$ , to measure absolute temperature, was mounted on the cell as close as possible to the

scattering site. This thermometer was calibrated (Cryogenic Calibrations, Pitchott, England) according to the International Practical Temperature Scale (1968) to a claimed accuracy of  $\pm 8\text{mK}$ . The temperature measurements were made on a null detector (Medistor Model A75A) before and after each spectrum.

The gas inlet tube was externally connected to the sample gas supply as well as to a series of three Bourdon tube gauges which permitted accurate (0.2% to 0.5%) measurements of pressure in three stages (0-60 psi, 0-300 psi and 0-1000 psi) over the range from 1 to 50 bars. A pressure fuse of the rupture-disc type was installed to prevent accidental pressure build-up in excess of 70 bars.

### 3.6 Cryostat

The scattering cell was suspended in the tail section of a variable temperature cryostat (Andonian Associates, Model IV-4-0500) (Fig. 3.4) by way of a vacuum O-ring seal whose flexibility permitted some vertical and rotational adjustments for alignment purposes. The gas inlet tube was surrounded by an annular exchange gas chamber, G, and was insulated from it by a vacuum space (H). The exchange gas chamber was closed at the end by relatively large brass ring, which served as a heat sink for the system. The gas exchange chamber was surrounded by concentric liquid nitrogen coolant reservoir. The thermal contact between the liquid coolant (J) and the exchange gas was attained by a common wall. The outer reservoir (F) which was not used in the present experiment was replaced by an aluminum radiation shield.

FIGURE 3.4

## The Cryostat.

- A Electrical feedthrough.
- B Exchange gas port.
- C Nitrogen fill and vent.
- D Nitrogen vent.
- E Nitrogen fill.
- F Nitrogen reservoir (outer).
- G Exchange gas chamber.
- H Vacuum gap.
- I Sample support tube.
- J Nitrogen reservoir (inner).
- K Outer tail section.
- L Nitrogen temperature radiation shield.
- M Heat sink.
- N Sample cell.
- O Quartz window (one of four).
- P Copper braids.

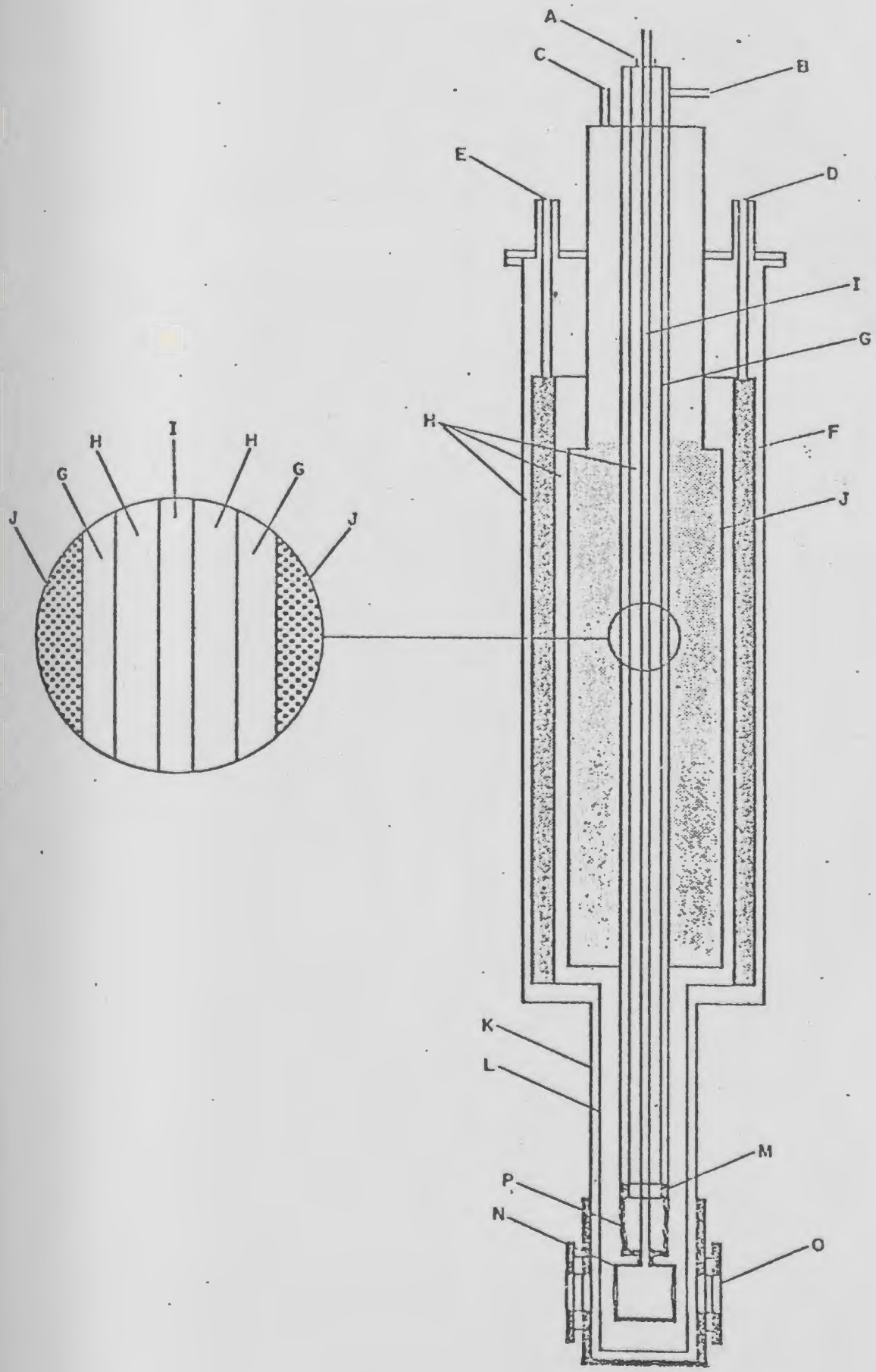


Fig. 3.4

The internal volume of the cryostat was evacuated to  $10^{-5}$  torr by a portable vacuum system (Diffusion-Rotary Pump, Alcatel Model 5477). The exchange chamber was filled with oxygen gas which established a thermal link between the cell and main coolant (liquid nitrogen) reservoir of the cryostat. Oxygen gas in the exchange chamber condenses on the cold wall of the liquid nitrogen reservoir (J) and falls to the heat sink (M) to which the cooling braids of the cell are connected. The sink temperature goes down on evaporation of the oxygen droplets. Coarse control of the cooling power, thus provided to the cell, could be achieved by varying the pressure of the heat exchange gas (oxygen). This way, temperature down to 85K was easily obtained, while temperatures down to 78K were achieved by lowering the vapour pressure of the coolant via a vacuum pump.

## CHAPTER 4

RESULTS AND DISCUSSION4.1 Procedure

The sample gases used were supplied by Matheson Gas Product with purities of 99.9995% for  $N_2$ , 99.99% for  $O_2$  and CO. The pressure of the gas in the cell was recorded with an accuracy of  $\sim 1$  psi by Bourdon tube gauges as described in Chapter 3. The temperature stability was controlled using a GaAs thermometer and monitored with a platinum resistance thermometer indicating a stable temperature within about  $\pm 0.02K$ .

The experimental technique used is described in Chapter 3. Since the DAS-1 needs a spectral line with at least 10 counts/sweep for drift stabilization and finesse optimization, the laser line was chosen as a reference line rather than the Raman line itself because of its very weak intensity. With the help of a shutter mechanism shown in Fig. (3.1) a small percentage of the laser light was allowed to pass through the Fabry-Perot interferometer for a brief interval of the sweep, so that only one order of the laser line could be seen on the CRT screen of the DAS-1, which was then used as a reference line. The amplitude of the ramp voltage was chosen such that two orders of the Raman band could be recorded. Use of the "Segmented Time Base" option of the DAS-1 was a great help in saving time in recording the Raman spectrum because of its very weak intensity. After the optics were adjusted for maximum finesse, the drift stabilization and finesse optimization windows were centered on the reference laser line.

To study the frequency shift and line-width dependence on density near the critical temperatures of  $N_2$ ,  $O_2$  and CO gases,

Raman spectra were accumulated in the DAS-1 memory normally for about 1 hr, for different pressures keeping the temperature constant. A few sets of temperatures were taken for all the three gases. Being very close to the critical point it was necessary to wait about 1 hr to reach thermal equilibrium and run another spectrum after changing the gas pressure.

Actual measurements of the spectra were made directly on the DAS-1 CRT screen using the readout features described in Chapter 3. For the frequency shift measurements it was made sure that for a given temperature the order of the Raman spectra remained the same for different gas pressures except for slight change in peak positions due to the density effect. The Bug was placed on each peak of a given spectrum and the channel number as well as the corresponding number of counts in that channel were recorded. Assuming the frequency shift of the Raman Q-branch to be zero for the highest possible density that could be reached, by reducing the density the Raman Q-branch was shifted from the previous position. By recording the channel numbers of the two peaks of successive orders of the Raman line, the number of channels the Raman line shifted by reducing the density, was measured.

Figure 4.1 shows a typical Raman Q-branch spectrum for two different densities. The frequency shift was calculated as follows:

$$\Delta v_{\text{in ch\#}} = \{(T_1 - T_2) + (T_1' - T_2')\} / 2$$

$$\Delta v = (\{(T_1 - T_2) + (T_1' - T_2')\} / 2 (T_1 - T_1')) \times \text{SFR (GHz.)}$$

FIGURE 4.1

Typical Raman Q-branch spectra for two densities with the same reference line. The spectrum shown with dashes is at density  $\rho_1$  while the other spectrum is at density  $\rho_2$ . Various measurements made to determine the frequency shift and line width are shown.

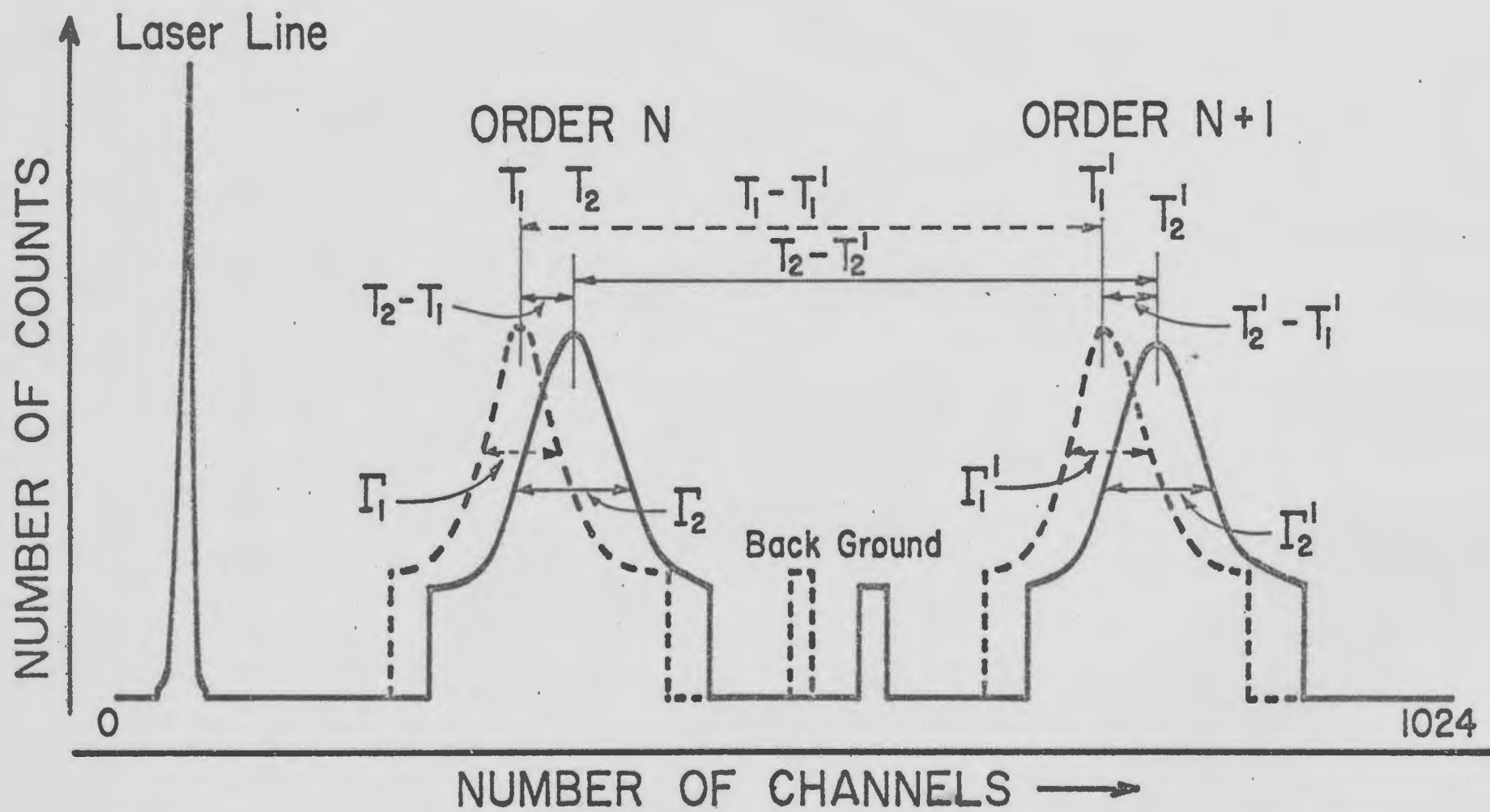


Fig. 4.1

Data for the Raman frequency shifts were collected for different densities as described above. Considering the shift to be zero for the highest gas density (approached), the gas pressure was reduced in succession down to a density as low as  $\sim 10$  Amagat for all three ( $N_2$ ,  $O_2$  &  $CO$ ) gases till the Raman Q-branches showed asymmetry and also became very weak. This frequency shift was plotted against density and was extrapolated for zero density. The origin of the frequency shift scale was, then, shifted to the zero density value.

For the line-width measurements, the full width at half maximum (FWHM) was found from the spectrum recorded on the CRT screen of the DAS-1. The Raman line peak counts were added to the background counts and for half of this sum one position on each side of the peak was located in channel numbers. The difference between these channel numbers gave the FWHM in number of channels. This way the width was found for both the orders and an average of the two was taken. FWHM was converted in GHz as follows:

$$\Gamma(\rho_1) = \{(\Gamma_1 + \Gamma_1')/2(T_1 - T_1')\} \times \text{SFR} \text{ GHz}$$

similarly,

$$\Gamma(\rho_2) = \{(\Gamma_2 + \Gamma_2')/2(T_2 - T_2')\} \times \text{SFR} \text{ GHz}$$

where,  $\Gamma(\rho)$  is the FWHM at density  $\rho$ . The instrumental width was determined from the width of the reference laser line by the same above procedure. In this experiment this width is mainly due to the resolution of the Fabry-Perot interferometer and was about 1.8 GHz which was always less than 20% of the measured Raman line width  $\Gamma(\rho)$ , except for very high pressures in case of  $N_2$ . This instrumental width was subtracted from the  $\Gamma(\rho)$  to give corrected Raman line-width (48).

## 4.2 Data

The experimental results for relative Raman shift and line width (FWHM) are presented in Tables (4.2-4.4) against density ( $\rho$ ). These data for the relative frequency shift ( $\nu - \nu_0$ ) and the line width ( $\Gamma$ ) were plotted against density ( $\rho$ ) and reduced density ( $\rho/\rho_c$ ) and represented graphically in Figs. (4.2-4.8), showing the anomaly due to the critical effects. The quantity  $\rho_c$  is the critical density given in Table (4.1).

Gas densities were determined using the published PVT data for  $O_2$ (45) while the equations of state were used for  $N_2$ (46) and CO (47). It is estimated from the scatter of the data that the random experimental errors in measurements of relative frequency shift and line width are about 2% and 7% respectively. The critical fluctuations as well as the experimental errors in determination of density may cause a considerable uncertainty in density measurements. It is estimated that this uncertainty in density may be as high as 15% (particularly in the case of CO) close to the critical density.

The anomaly, which occurs close to the critical temperature ( $T_c$ ), is quite reproducible and it is very unlikely that the experimental errors could account for this anomaly. It is the qualitative features of the observations that are to be emphasized in this thesis.

## 4.3 Discussion

In the treatment to follow those ideas pertaining to the interpretation of the observed anomaly are due mainly to Clouter

TABLE 4.1

List of critical density ( $\rho_c$ ) and critical temperature ( $T_c$ ) and the calculated values of  $(\nu_Q - \bar{\nu}_Q)$  for  $N_2$ ,  $O_2$  and  $CO$  gases.

---

Gas	$\rho_c$ (Amagat)	$T_c$ (K)	$(\nu_Q - \bar{\nu}_Q)$ (GHz)
$N_2$	250.9	126.25	12.43
$O_2$	304.2	154.57	17.74
$CO$	239.6	132.85	12.67

---

TABLE 4.2

List of the relative Raman frequency shift ( $\nu - \nu_0$ ), and the Raman line-width (FWHM),  $\Gamma$ , data at different densities ( $\rho$ ) for Nitrogen ( $N_2$ ) at three different temperatures.

a) For  $T - T_c = 0.73K$

b) For  $T - T_c = 1.80K$

and c) For  $T - T_c = 5.73K$

a)  $T - T_c = 0.73\text{K}$ 

$\rho^*$ (Amagat)	$\rho/\rho_c^*$	$\nu - \nu_0$ (GHz)	$\Gamma$ (GHz)
0	0	0	—
16.25	0.065	-6.1	9.5
21.83	0.087	-7.6	9.9
29.02	0.116	-10.2	9.4
40.17	0.160	-12.4	9.3
51.78	0.206	-14.6	10.4
66.41	0.265	-17.2	8.9
78.94	0.315	-19.2	7.9
95.20	0.379	-21.4	—
95.20	0.379	-21.4	8.1
110.29	0.440	-23.1	8.5
142.8	0.569	-24.7	8.9
189.2	0.754	-26.5	8.2
235.7	0.939	-29.5	9.4
258.9	1.032	-31.6	10.9
269.3	1.074	-33.9	11.7
284.4	1.134	-41.5	12.5
296.0	1.180	-45.3	8.1
318.1	1.268	-46.8	—
349.4	1.393	-47.7	5.3
366.8	1.462	-48.5	5.4
377.3	1.504	-48.5	5.6
377.3	1.504	-48.5	5.2
389.4	1.552	-48.7	5.0

Continued

$\rho$ (Amagat)	$\rho/\rho_C$	$\nu-\nu_0$ (GHz)	$\Gamma$ (GHz)
397.0	1.583	-49.0	4.6
402.8	1.606	-50.1	4.2
407.5	1.624	-50.5	4.6
412.6	1.644	-50.7	4.1
416.1	1.658	-50.9	3.9
419.1	1.670	-51.1	3.3
419.1	1.670	-51.1	4.1
423.7	1.689	-51.3	3.5
427.5	1.704	-51.3	3.5
430.0	1.714	-51.5	3.5
433.5	1.728	-51.4	3.7
436.1	1.738	-51.7	3.8
438.8	1.749	-52.2	3.7
441.6	1.760	-52.6	3.4
444.2	1.770	-52.3	3.7
446.5	1.780	-52.5	3.5
448.8	1.788	-52.8	3.0
451.1	1.798	-53.1	3.3
453.2	1.806	-53.1	2.9

\* See page 40 for discussion of errors.

b)  $T - T_c = 1.80\text{K}$

$\rho$ (Amagat)	$\nu - \nu_0$ (GHz)	$\Gamma$ (GHz)
0	0	—
13.23	-4.7	—
19.74	-6.8	10.0
29.02	-9.9	9.8
39.01	-11.9	8.8
51.08	-13.8	8.0
64.32	-16.0	8.3
80.11	-18.6	8.3
99.84	-21.1	8.6
120.7	-24.1	8.7
120.7	-24.1	9.1
135.8	-25.9	9.1
150.9	-27.9	9.0
164.8	-29.1	10.1
197.4	-30.7	10.8
222.9	-32.5	11.6
236.8	-35.4	12.3
250.8	-39.1	11.3
268.2	-41.7	10.0
285.6	-43.3	8.5
319.3	-45.4	7.3
344.8	-46.2	7.2
365.2	-48.0	5.5

continued

$\rho$ (Amagat)	$\nu - \nu_0$ (GHz)	$\Gamma$ (GHz)
379.9	-49.0	5.6
394.3	-50.1	5.2
399.8	-50.1	4.8
409.8	-51.2	4.2
417.5	-51.7	3.8
423.7	-52.4	3.9
426.3	-52.5	3.8
433.7	-52.9	3.8
438.1	-53.4	3.5
442.3	-53.7	3.3

c)  $T - T_c = 5.73\text{K}$ 

0	0	—
12.77	-3.5	9.5
16.72	-6.4	10.4
28.56	-8.5	—
37.38	-10.7	8.7
47.60	-13.0	9.7
59.91	-14.9	8.7
76.16	-17.3	7.6
93.34	-19.4	7.7

continued

---

$\rho$ (Amagat)	$\nu - \nu_0$ (GHz)	$\Gamma$ (GHz)
113.3	-22.4	7.7
113.3	-22.4	—
133.7	-25.9	8.8
149.1	-27.4	8.9
166.0	-29.2	9.2
186.9	-31.4	8.4
204.3	-33.4	9.3
228.7	-35.5	9.7
257.8	-38.6	9.2
270.5	-39.4	8.6
291.4	-41.9	7.7
319.3	-43.7	6.7
340.6	-45.4	6.2
355.7	-46.3	5.8
366.9	-47.1	5.5
376.2	-47.9	5.2
385.4	-48.3	5.6
393.3	-49.1	4.7
399.6	-49.9	4.2
403.3	-50.5	4.1

TABLE 4.3

List of the relative Raman frequency shift,  $(\nu - \nu_0)$ , and the Raman line-width (FWHM), data at different densities ( $\rho$ ) for oxygen ( $O_2$ ) at three different temperatures.

- a) For  $T - T_c = 0.12K$
- b) For  $T - T_c = 0.95K$
- and c) For  $T - T_c = 7.87K$

a)  $T - T_c = 0.12\text{K}$ 

$\rho$ (Amagat)	$\rho/\rho_c$	$\nu - \nu_0$ (GHz)	$\Gamma$ (GHz)
0	0	0	—
17.9	0.059	-7.6	—
27.2	0.089	-9.8	14.9
34.1	0.112	-14.2	14.8
45.6	0.150	-15.9	15.0
54.6	0.180	-18.7	13.7
65.0	0.214	-20.4	13.7
76.2	0.251	-20.6	14.0
92.5	0.304	-25.8	14.1
108.7	0.357	-28.6	15.5
123.3	0.405	-30.6	14.7
139.0	0.457	-32.9	14.9
151.9	0.499	-34.7	15.4
165.9	0.545	-36.8	15.1
190.6	0.627	-38.0	16.9
215.2	0.707	-39.7	16.9
241.0	0.792	-41.3	17.8
262.3	0.862	-42.9	18.1
276.3	0.908	-44.4	18.0
283.6	0.932	-46.7	18.8
289.2	0.951	-49.9	20.2
294.8	0.969	-53.6	20.3
299.9	0.986	-55.8	18.0
312.8	1.028	-59.1	13.2

continued

$\rho$ (Amagat)	$\rho/\rho_c$	$\nu-\nu_0$ (GHz)	$\Gamma$ (GHz)
323.4	1.063	-60.2	12.2
332.9	1.094	-60.8	12.0
343.6	1.130	-61.5	11.3
367.7	1.209	-61.8	11.1
396.7	1.301	-62.9	10.4
433.3	1.424	-63.6	9.4
442.8	1.456	-64.4	9.4
450.6	1.481	-64.8	8.1
458.5	1.507	-65.3	8.1
465.2	1.529	-66.2	8.3
471.4	1.550	-66.5	7.9
475.9	1.564	-66.7	6.4
479.8	1.577	-67.1	7.1
483.2	1.588	-67.7	7.5
486.0	1.598	-67.7	6.8

b)  $T-T_c = 0.95K$ 

$\rho$ (Amagat)	$\nu-\nu_0$ (GHz)	$\Gamma$ (GHz)
0	0	—
16.25	-6.9	16.8
26.34	-10.2	16.0

continued

---

$\rho$ (Amagat)	$\nu - \nu_0$ (GHz)	$\Gamma$ (GHz)
34.19	-13.0	14.8
44.84	-15.6	14.6
54.37	-17.7	15.1
64.46	-19.3	15.7
72.30	-21.2	15.3
88.00	-24.4	14.6
102.6	-26.7	14.3
116.6	-28.7	15.1
127.8	-30.7	14.8
143.5	-32.8	15.1
155.3	-33.9	14.9
163.7	-35.3	15.7
172.6	-36.7	16.1
187.2	-38.3	15.8
195.6	-39.9	17.3
228.8	-41.7	17.6
272.4	-43.8	17.9
294.8	-45.4	19.0
309.4	-48.7	18.6
313.9	-49.4	19.2
320.6	-50.0	18.4
329.6	-53.7	17.0
337.4	-55.1	16.8

continued

$\rho$ (Amagat)	$\nu - \nu_0$ (GHz)	$\Gamma$ (GHz)
341.9	-56.4	15.9
345.3	-56.5	15.6
348.6	-57.8	15.4
353.1	-58.2	14.6
357.6	-57.9	13.9
392.9	-60.6	11.3
408.0	-61.4	11.1
417.0	-61.8	10.8
420.4	-62.1	10.8
426.5	-62.6	10.5
438.9	-63.9	8.9
447.8	-64.3	8.1
454.6	-64.8	8.6
464.7	-66.1	7.8
471.4	-66.6	7.1

c)  $T - T_c = 7.87K$ 

0	0	—
13.0	-5.6	17.5
19.6	-7.8	17.5
27.0	-10.0	16.4
34.7	-12.5	16.5

continued

---

$\rho$ (Amagat)	$\nu - \nu_0$ (GHz)	$\Gamma$ (GHz)
40.7	-14.2	16.0
45.5	-15.2	16.4
51.9	-16.4	15.3
61.0	-18.9	15.2
70.3	-20.7	15.1
78.8	-22.2	14.9
89.8	-24.2	15.3
99.0	-26.1	15.5
107.5	-27.3	15.4
116.5	-28.7	14.4
125.0	-30.4	15.6
134.0	-31.7	15.5
142.0	-32.5	14.4
152.5	-33.9	15.4
162.5	-35.1	14.9
170.0	-36.2	14.7
178.0	-37.2	15.1
187.0	-38.6	14.8
187.0	-38.6	15.1
193.0	-39.8	14.8
200.5	-40.0	16.1
209.5	-41.4	15.5
224.5	-43.0	15.5

continued

---

$\rho$ (Amagat)	$\nu - \nu_0$ (GHz)	$\Gamma$ (GHz)
238.0	-44.4	15.6
247.0	-45.6	15.6
256.0	-46.6	15.1
270.5	-48.3	15.4
299.5	-51.8	15.0
318.8	-54.0	14.2

TABLE 4.4

List of the relative Raman frequency shift,  $(\nu - \nu_0)$ , and the Raman Line-width (FWHM),  $\Gamma$ , data at different densities ( $\rho$ ) for carbon monoxide (CO) at four different temperatures.

- a) For  $T - T_c = 0.13\text{K}$
- b) For  $T - T_c = 3.46\text{K}$
- c) For  $T - T_c = 8.92\text{K}$
- and d) For  $T - T_c = 17.03\text{K}$

a)  $T - T_c = 0.13\text{K}$ 

$\rho$ (Amagat)	$\rho/\rho_c$	$\nu - \nu_0$ (GHz)	$\Gamma$ (GHz)
0	0	0	—
10.20	0.043	-5.6	7.9
22.50	0.094	-8.7	9.8
36.00	0.150	-11.5	8.3
48.4	0.202	-14.3	8.2
62.00	0.258	-16.0	8.5
73.20	0.306	-18.0	8.5
84.50	0.353	-19.7	8.5
98.30	0.410	-21.6	9.1
113.2	0.473	-23.5	9.3
123.9	0.517	-24.9	10.0
132.5	0.553	-26.0	10.7
142.2	0.594	-26.7	11.3
142.2	0.594	-27.2	10.7
153.4	0.640	-28.4	12.3
165.3	0.690	-30.1	12.9
250.0	1.043	-31.8	15.5
305.0	1.273	-34.4	15.9
311.3	1.299	-38.7	17.2
313.4	1.308	-42.8	13.6
317.1	1.323	-43.3	13.0
323.2	1.349	-44.9	12.4
333.2	1.391	-46.3	10.5

continued

$\rho$ (Amagat)	$\rho/\rho_C$	$\nu-\nu_0$ (GHz)	$\Gamma$ (GHz)
340.0	1.419	-46.6	10.0
350.9	1.465	-47.9	9.4
360.5	1.505	-48.6	9.2
370.8	1.548	-49.5	8.6
377.1	1.574	-50.0	8.6
384.0	1.603	-50.4	8.0
390.8	1.631	-50.9	7.8
397.1	1.657	-51.6	7.8
402.3	1.679	-51.9	7.5
407.1	1.699	-52.5	7.6
412.2	1.720	-52.8	7.2
416.5	1.738	-53.3	7.1
420.7	1.756	-53.6	6.9
424.7	1.773	-54.0	6.8

b)  $T-T_C = 3.46K$ 

$\rho$ (Amagat)	$\nu-\nu_0$ (GHz)	$\Gamma$ (GHz)
0	0	—
9.90	-5.3	—
17.60	-7.9	8.6
24.30	-9.3	9.2
31.40	-11.2	9.0

continued

---

$\rho$ (Amagat)	$\nu - \nu_0$ (GHz)	$\Gamma$ (GHz)
38.80	-12.2	9.1
47.20	-14.1	8.7
56.20	-15.7	8.4
67.00	-17.6	7.9
77.30	-19.0	8.4
85.60	-20.1	8.6
85.60	-20.1	8.8
95.00	-21.3	8.9
103.5	-22.3	9.2
113.2	-23.7	9.6
124.6	-25.1	10.0
136.3	-26.5	10.2
147.1	-28.1	10.7
164.1	-30.0	11.4
176.5	-31.3	12.7
194.4	-33.5	12.8
224.6	-36.8	13.4
242.4	-38.2	13.4
276.4	-41.4	12.1
285.1	-42.5	11.7
304.5	-44.2	10.4
321.7	-45.4	10.1
329.4	-46.1	9.7
338.1	-46.6	9.5

---

continued

---

$\rho$ (Amagat)	$\nu - \nu_0$ (GHz)	$\Gamma$ (GHz)
342.8	-46.8	9.3
350.9	-47.6	9.0
357.8	-48.1	8.8
363.5	-48.6	8.3
367.9	-49.1	8.4
372.8	-49.5	8.0
377.3	-49.9	7.8
380.4	-50.1	8.1
384.3	-50.5	7.4
388.0	-50.9	7.4
391.3	-51.4	7.4
394.5	-51.5	7.9
397.5	-51.7	7.6
397.5	-51.7	7.3
400.3	-52.1	7.5
400.3	-52.1	7.3
403.3	-52.5	7.4
406.2	-52.7	7.4
406.4	-52.6	6.9
408.5	-52.8	7.5

---

c)  $T - T_c = 8.92\text{K}$ 

$\rho$ (Amgat)	$\nu - \nu_0$ (GHz)	$\Gamma$ (GHz)
0	0	—
09.40	-5.4	10.2
18.00	-7.6	10.1
27.00	-10.0	8.9
35.70	-11.9	8.3
43.90	-13.7	8.4
53.00	-15.1	8.4
61.90	-16.5	8.4
70.60	-18.1	8.6
80.3	-19.5	8.8
90.40	-20.6	8.7
100.4	-22.3	9.1
111.7	-23.5	8.5
124.6	-25.3	9.1
139.6	-27.2	9.7
154.4	-28.8	10.0
171.8	-31.0	10.1
186.9	-32.5	10.5
205.5	-34.4	10.5
224.2	-36.4	11.0
236.5	-37.6	11.0
247.4	-38.8	11.0
264.2	-40.5	10.3

continued

$\rho$ (Amagat)	$\nu - \nu_0$ (GHz)	$\Gamma$ (GHz)
275.5	-41.6	10.4
282.4	-42.3	10.1
288.8	-42.7	10.0
296.9	-43.5	9.4
311.0	-44.8	9.0
326.8	-46.5	8.7
336.7	-47.5	8.3
345.0	-48.2	8.2
352.5	-48.7	8.2
359.2	-49.3	7.8

d)  $T - T_c = 17.03K$ 

0	0	—
15.70	-6.4	—
26.60	-9.1	10.2
37.60	-11.7	9.4
48.90	-13.6	8.0
59.30	-15.5	8.3
69.40	-17.0	8.4
80.20	-18.9	8.6
91.20	-20.5	8.5
102.9	-21.7	8.3
113.2	-23.2	8.9
124.4	-24.8	8.6

continued

---

$\rho$ (Amgat)	$\nu - \nu_0$ (GHz)	$\Gamma$ (GHz)
136.6	-26.0	8.7
150.0	-27.4	9.3
162.3	-29.0	8.6
176.8	-30.3	9.3
191.1	-32.1	8.9
204.3	-33.2	9.0
218.2	-34.9	9.3
229.9	-36.2	9.4
244.0	-37.8	8.9
254.7	-38.7	8.5
268.0	-39.4	8.8
277.9	-40.7	8.8

FIGURE 4.2

Plots of relative Raman frequency shift ( $\nu - \nu_0$ ) vs. density ( $\rho$ ) for  $N_2$  at three different temperatures,

i)  $T - T_c = 0.73K$

ii)  $T - T_c = 1.80K$

and iii)  $T - T_c = 5.73K.$

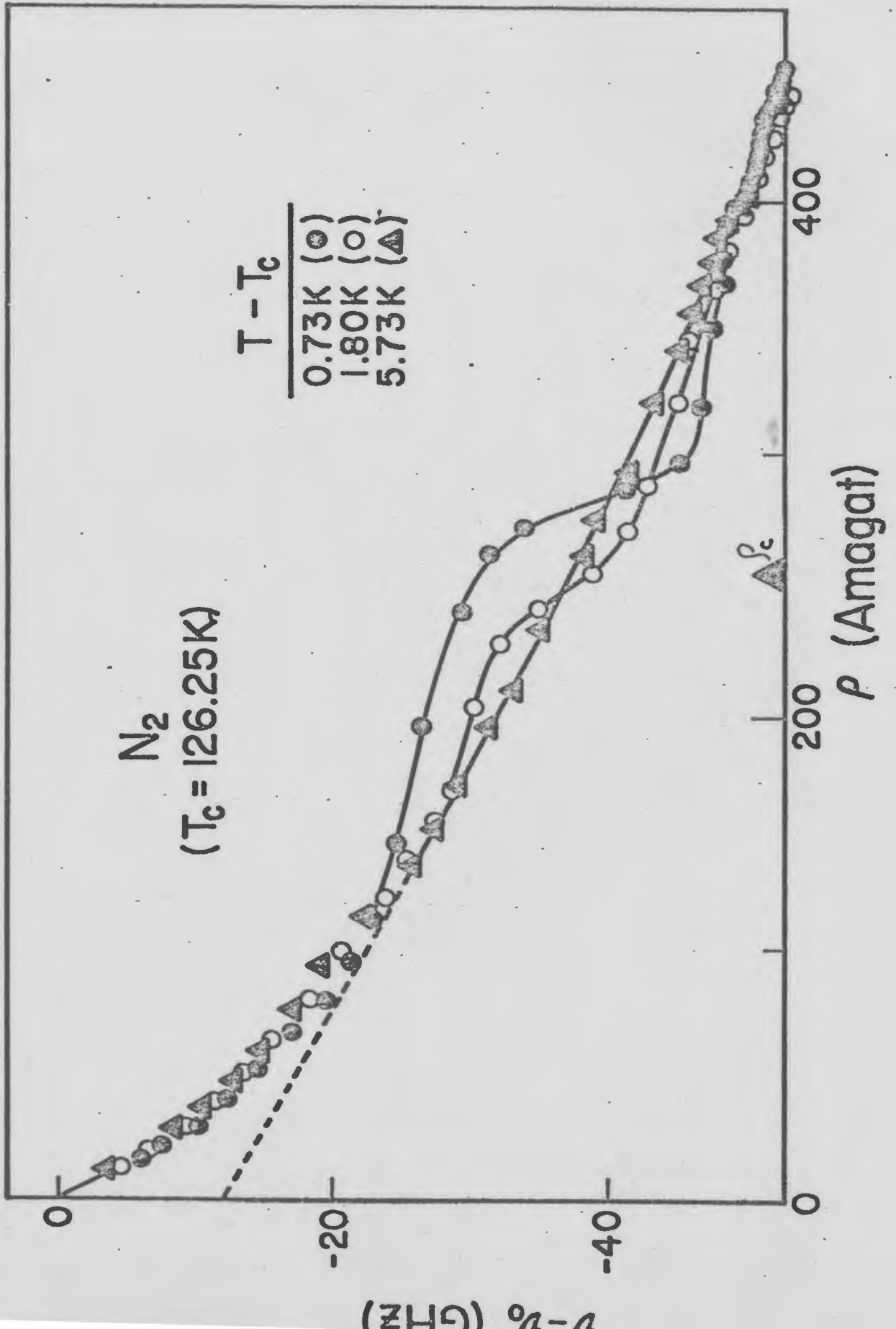


Fig. 4.2

FIGURE 4.3

Plots of relative Raman frequency shift  $(\nu - \nu_0)$  vs. density  $(\rho)$  for  $O_2$  at three different temperatures,

i)  $T - T_c = 0.12K$

ii)  $T - T_c = 0.95K$

and iii)  $T - T_c = 7.87K.$

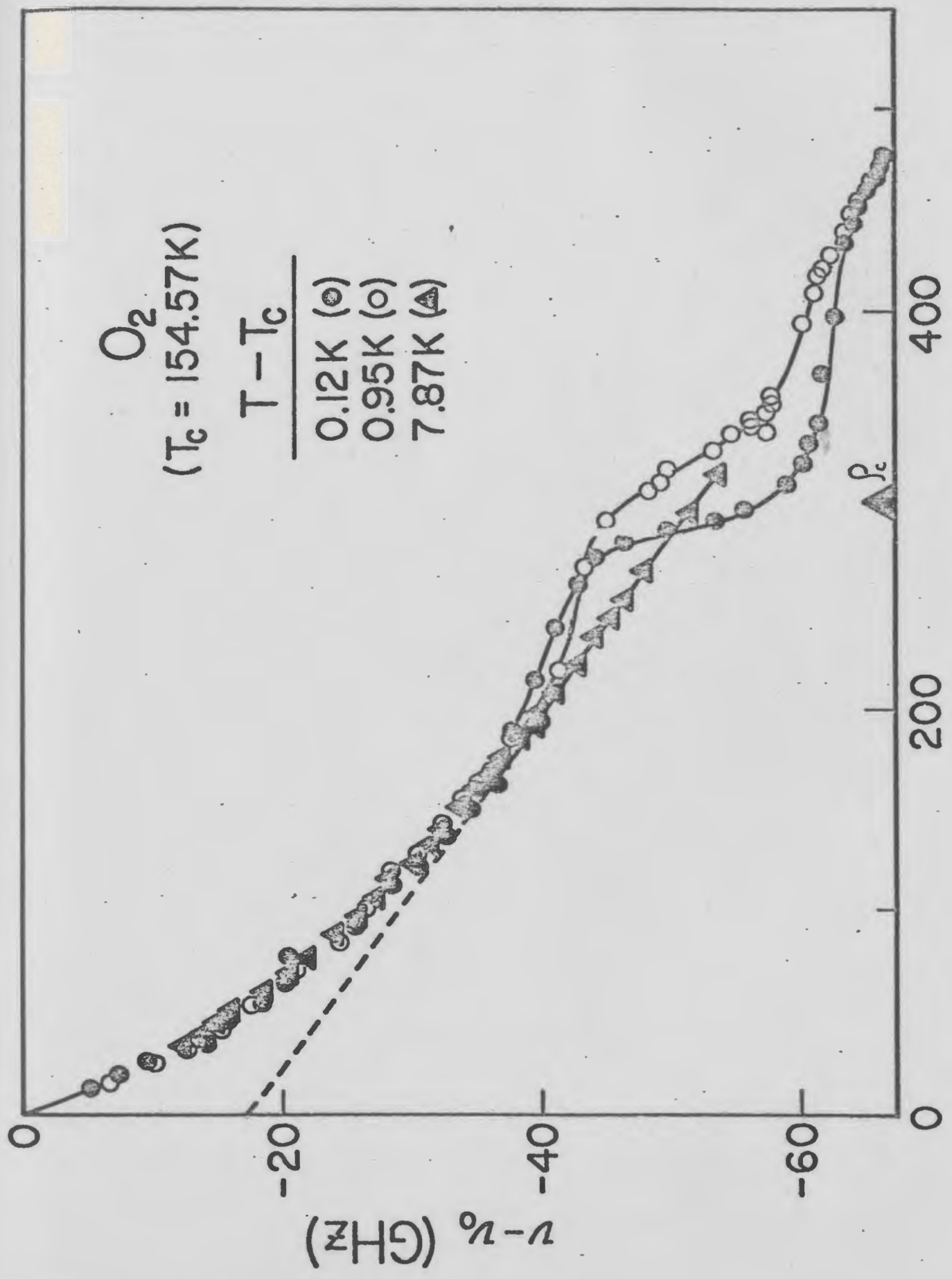


Fig. 4.3

FIGURE 4.4

Plots of relative Raman frequency shift ( $\nu - \nu_0$ ) vs. density ( $\rho$ ) for CO at three different temperatures,

i)  $T - T_c = 0.13\text{K}$

ii)  $T - T_c = 3.46\text{K}$

and iii)  $T - T_c = 8.92\text{K}.$

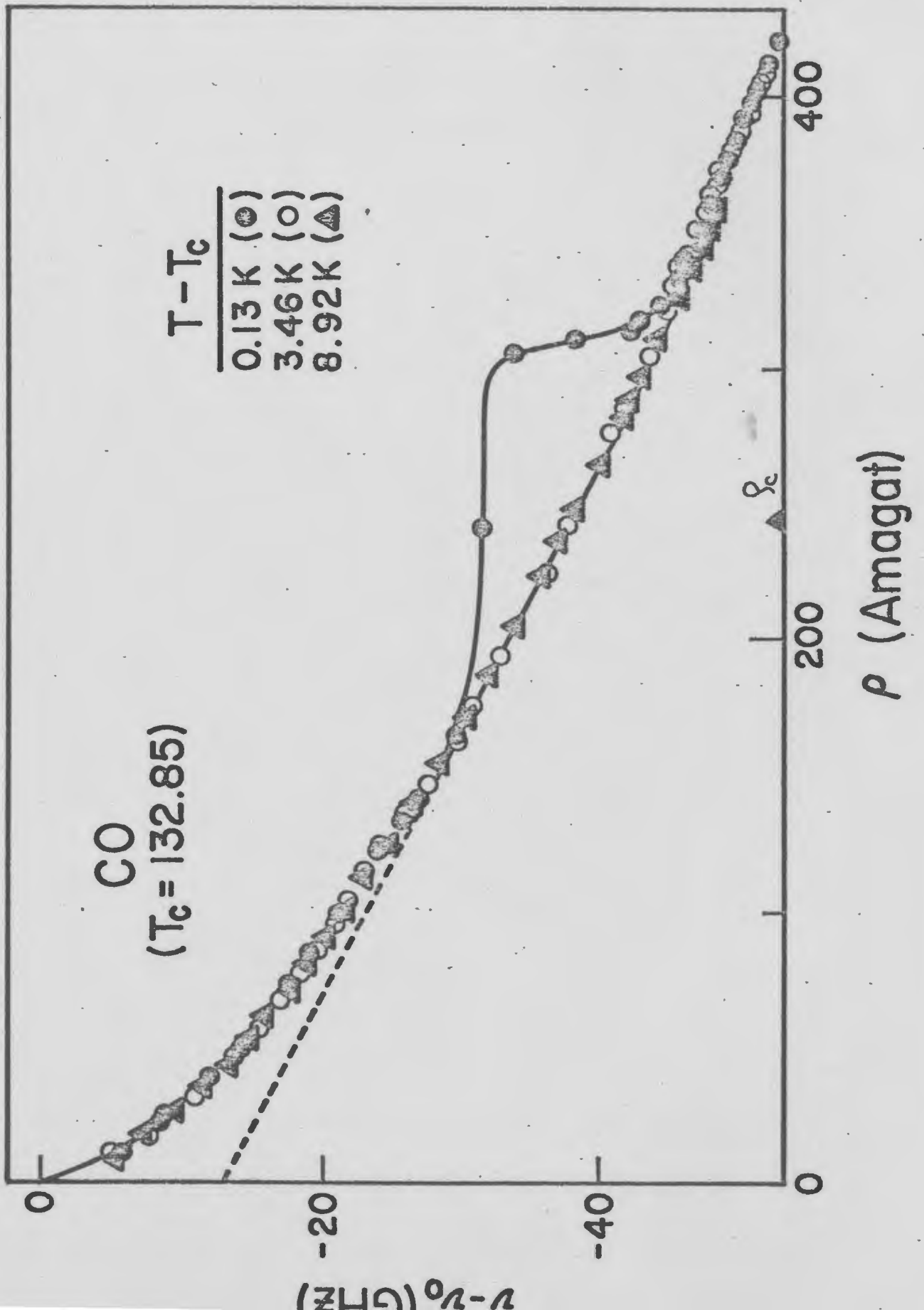


Fig. 4.4

FIGURE 4.5

Plots of the full-width at half maximum (FWHM),  $\Gamma$ , of the Raman Q-branch vs. density ( $\rho$ ) for  $N_2$  at three different temperatures,

i)  $T - T_c = 0.73K$

ii)  $T - T_c = 1.80K$

and iii)  $T - T_c = 5.73K.$

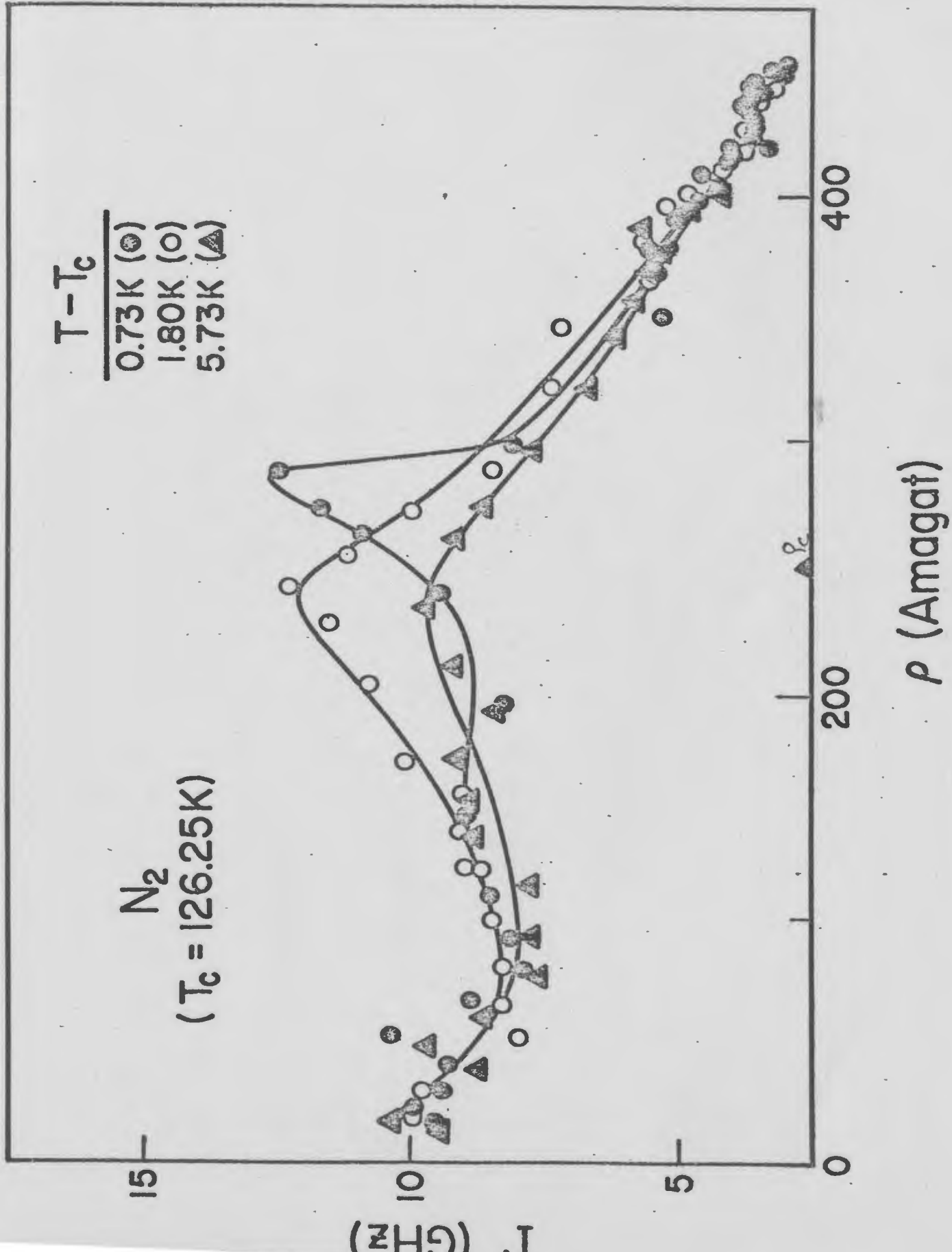


Fig. 4.5

FIGURE 4.6

Plots of the full-width at half maximum (FWHM),  $\Gamma$ , of the Raman Q-branch vs. density ( $\rho$ ) for  $O_2$  at three different temperatures,

i)  $T - T_c = 0.12K$

ii)  $T - T_c = 0.95K$

and iii)  $T - T_c = 7.87K.$

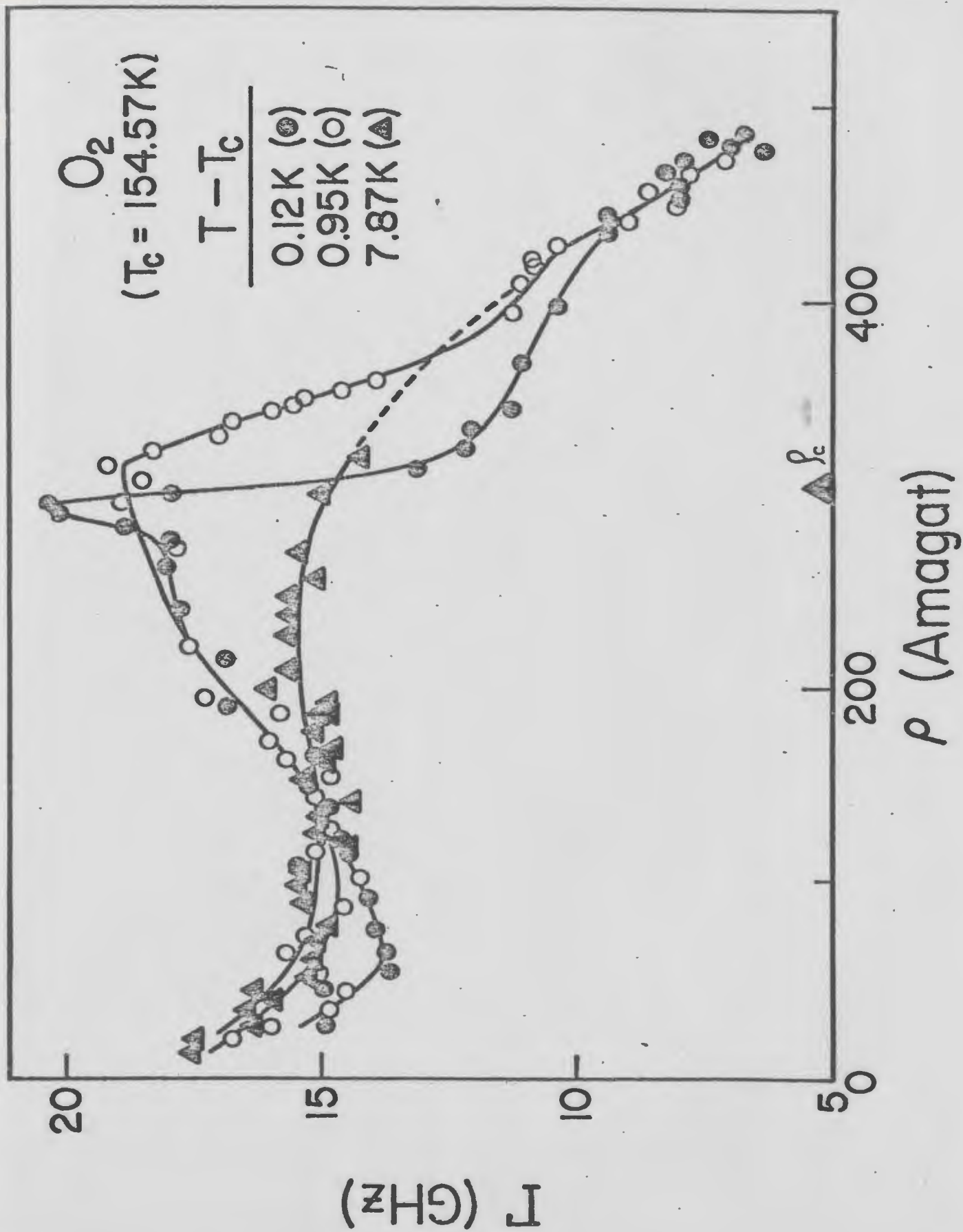


Fig. 4.6

FIGURE 4.7

Plots of the full-width at half maximum (FWHM),  $\Gamma$ , of the Raman Q-branch vs. density ( $\rho$ ) for CO at four different temperatures,

i)  $T - T_c = 0.13\text{K}$

ii)  $T - T_c = 3.46\text{K}$

iii)  $T - T_c = 8.92\text{K}$

and iv)  $T - T_c = 17.03\text{K}.$

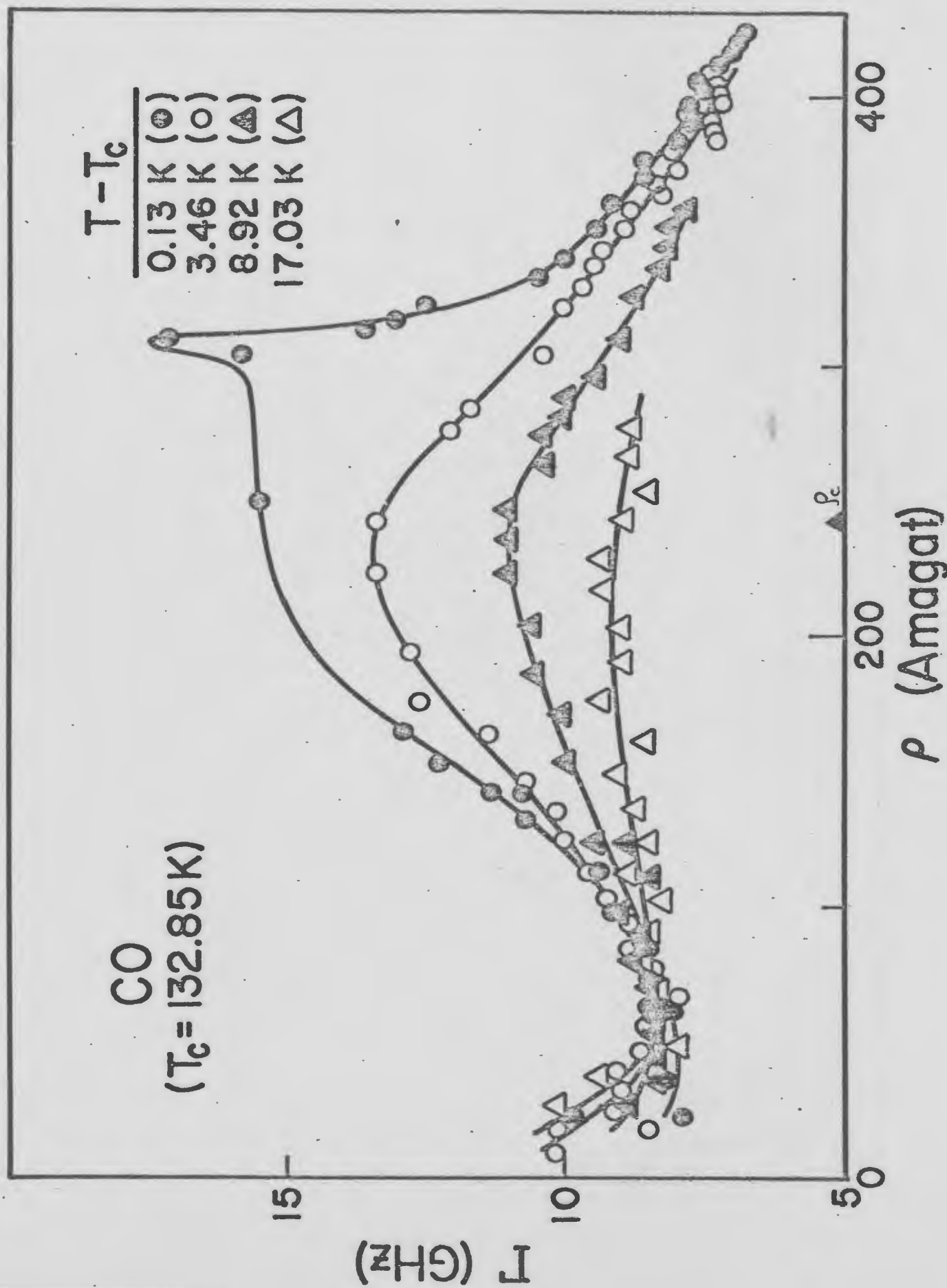


Fig. 4.7

FIGURE 4.8

(a) Plots of relative Raman frequency shift ( $\nu - \nu_0$ ) vs. density ( $\rho$ ) at temperatures  $T - T_c = 0.73\text{K}$ ,  $0.12\text{K}$  and  $0.13\text{K}$  for  $\text{N}_2$ ,  $\text{O}_2$  and  $\text{CO}$  respectively,  
and (b) corresponding plots of line-width,  $\Gamma$  vs. density ( $\rho$ ).

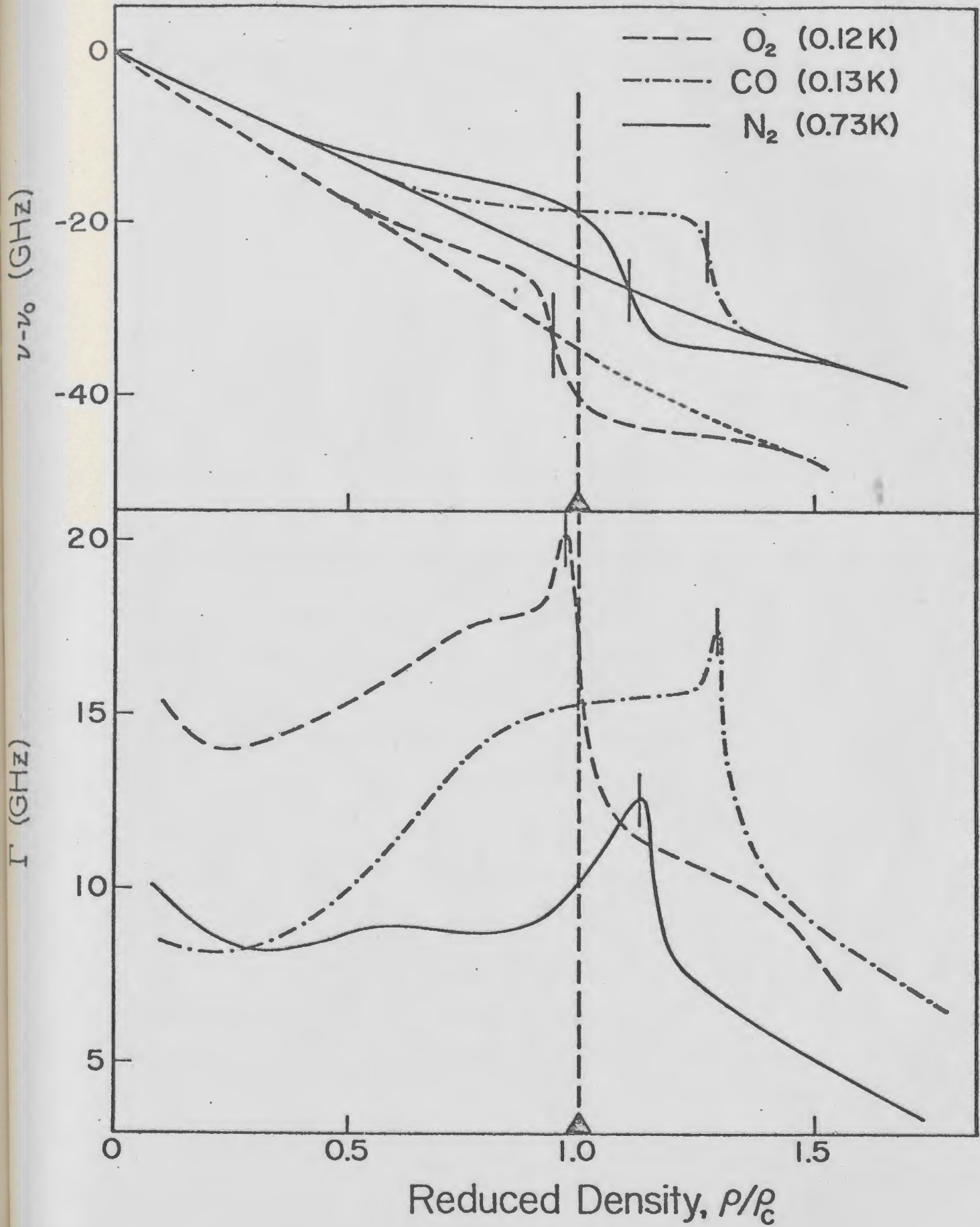


Fig. 4.8

et al. (49) and have previously been outlined elsewhere (see Appendix A).

(a) Relative Raman shift,  $\nu - \nu_0$

The relative Raman shift,  $\nu - \nu_0$ , is plotted against density ( $\rho$ ) and reduced density ( $\rho/\rho_c$ ) in Figs. (4.2-4.4, 4.8a) where  $\rho_c$  is the critical density. The quantity  $\nu \equiv \nu(\rho, T - T_c)$  is the vibrational Raman frequency at density  $\rho$  and temperature  $T$ , while the quantity  $\nu_0 \equiv \nu(0, T - T_c)$  is the vibrational Raman frequency for the free molecule ( $\rho = 0$ ), which is obtained by extrapolation as mentioned in the previous section. Since the temperature dependence of  $\nu(0, T - T_c)$  is negligible in the range of temperature considered in this work, it is reasonable to consider  $\nu(0, T - T_c) = \nu_0$ .

The distinct feature of the relative Raman shift curves is the anomalous behaviour near the critical density ( $\rho_c$ ) for temperatures close to the critical temperatures ( $T_c$ ). The anomaly diminishes away from the critical density and as the temperature is increased from the critical temperature the anomaly vanishes considerably faster as shown in Figs. (4.2-4.4). It is noted that the peak positions are shifted for  $N_2$  and CO from the critical density. The large uncertainty in measurement of density close to critical density (mentioned earlier) may account for this shift, and the quantity  $\rho_{cc}$ , to be defined later, should perhaps be close to critical density ( $\rho_c$ ). Another interesting feature of the Figs. (4.2-4.4) is the non-linear behavior at densities  $\rho < 150$  Amagats.

It was found by May et al. (10) for  $H_2$  (where the Q-branch components are well resolved) that for low densities ( $\rho < 300$  Amagats) the vibrational Raman frequency is proportional to the density.

One can expect a departure from this behavior in the present case (in case of  $N_2$ ,  $O_2$ , & CO where Q-branch components are unresolved) because of the "motional narrowing" effect discussed in Chapter 2. The unresolved Raman Q-branch is highly asymmetrical and this asymmetry reduces with increase in density as a result of the motional narrowing. At high density ( e.g.  $\rho > 150$  Amagat in present case) the band is highly symmetrical. There is a frequency shift of the peak associated with this process in addition to the shift due to perturbations in the vibrational frequency. This shift, given by  $(\nu_Q - \bar{\nu}_Q)$  as shown in Chapter 2, is responsible for the observed non-linear behavior of  $\nu - \nu_0$  in the region  $\rho < 150$  Amagat. At the same time it can be noticed from the Figs. (4.2-4.4) that a linear behavior of  $\nu - \nu_0$  is exhibited for densities  $\rho > 150$  Amagat, for the temperatures where critical effects are not evident. A direct effect of intermolecular interaction upon the vibrational frequency is represented by a linear extrapolation of  $\nu - \nu_0$  in the region  $\rho > 150$  Amagat, shown in Figs. (4.2-4.4) by dashes, considering the facts cited above. The calculated values for  $(\nu_Q - \bar{\nu}_Q)$  is given in Table (4.1) for  $N_2$ ,  $O_2$  and CO, which is the difference between the observed frequency shift and the linearly extrapolated value at  $\rho = 0$ . After this extrapolation, it is easy to see that apart from the anomaly the rest of the  $\nu - \nu_0$  vs  $\rho$  curve is explainable on the basis of the equation (2.1). It has to be emphasized that it is the linear term in equation (2.1) which is more important in the present situation with a small contribution due to the second, quadratic, term at high density which is evident from the curvature of the  $N_2$  and CO curves at high densities and temperatures.

To account for the anomaly a quantity  $\Delta\nu$  is defined as

$$\Delta\nu \equiv \nu(\rho, T-T_c) - \nu(\rho, T_M-T_c) \quad (4.1)$$

where,  $T_M$  stands for the temperature farthest from  $T_c$  (in this experiment) and  $T$  is any temperature between  $T_c$  and  $T_M$ . This quantity ( $\Delta\nu$ ) represents the difference in relative Raman shifts between the temperatures  $T$  and  $T_M$ . It has positive as well as negative values for  $O_2$  and  $N_2$  at  $T-T_c = 0.12K$  and  $T-T_c = 0.73K$  respectively, while it has only positive values for  $CO$  at all temperatures (Fig. (4.4)) and at other higher temperatures for  $O_2$  and  $N_2$  (Figs. (4.2, 4.3)). The relative Raman shift on the basis of equation (2.1) can be written as

$$\nu - \nu_0 = \sum_n a_n(T) \rho^n \quad (4.2)$$

Before an attempt is made to explain the anomaly one should consider the short-range nature of the intermolecular interactions with a range parameter of order 1 nm (44) and the large density fluctuations close to the critical temperature. Based on these facts it is convenient to introduce the idea of 'local density',  $\rho_{loc}$ , which corresponds to a volume of  $(1 \text{ nm})^3$ . It is the local density to which a single Raman scattering event is sensitive rather than the bulk density. With the introduction of the 'local density' idea and the density fluctuations near  $T_c$ , one can think of a density distribution function  $P(\rho_{loc})$ . The relative Raman shift in the critical region can be given, on the basis of equation (4.2), by

$$\nu - \nu_0 = \sum_n a_n(T) \langle \rho_{loc}^n \rangle \quad (4.3)$$

where,  $\langle \rangle$  means average over  $P(\rho_{loc})$ . From the Figs. (4.2-4.4), it is noted that apart from the anomaly the curves for different temperatures overlap quite nicely. This indicate negligible temperature dependence of  $a_n(T)$  in the present case, and it is consequently assumed  $a_n(T) \rightarrow a_n$  for small  $n$ . Then the quantity  $\Delta v$  can be written as

$$\Delta v = (v-v_0)_T - (v-v_0)_{T_M} = \sum_n a_n \langle \rho_{loc}^n \rangle - \sum_n a_n \rho^n$$

$$\text{or } \Delta v = \sum_n a_n (\langle \rho_{loc}^n \rangle - \rho^n) \quad (4.4)$$

To see whether this expression can account for the positive as well as negative values of  $\Delta v$ , at least a few orders of equation (4.4) have to be considered. The first order is found to be zero, as

$$\Delta v_1 = a_1 (\langle \rho_{loc} \rangle - \rho) = 0$$

Since, the average of local density is nothing but the bulk density. The second order gives,

$$\Delta v_2 = a_2 (\langle \rho_{loc}^2 \rangle - \rho^2) = a_2 M_2 \geq 0$$

where,  $M_2$  is the second moment of the density distribution which is always positive, and the experimental data indicate  $a_2 > 0$ .

Similarly, the third order gives,

$$\Delta v_3 = a_3 (\langle \rho_{loc}^3 \rangle - \rho^3) = 2a_3 \rho M_2 + a_3 M_3 \geq 0 \text{ or } \leq 0$$

where,  $M_3 = \langle (\rho_{loc} - \rho)^3 \rangle$  is the third moment which can be either positive or negative, while the sign of  $a_3$  is indeterminate.

Therefore, the contribution to  $\Delta v$  due to three orders is,

$$\Delta\nu = (a_2 + 3a_3\rho)M_2 + a_3M_3 \geq 0 \text{ or } \leq 0$$

and one must go at least this far to obtain an expression which predicts possible negative values of  $\Delta\nu$ . It can thus be inferred that non-zero values of  $M_3$  play a key role in this respect. It is now necessary to emphasize that from the data of relative Raman shift it is the constant  $a_1$  which is most important and consequently can be determined accurately. The higher order constants ( $a_3$  in particular) are almost impossible to determine accurately from the data. Furthermore, it is not possible to say how many orders are needed to adequately account for the positive as well as negative  $\Delta\nu$ .

At this point it is clear that if the anomaly is to be interpreted (even if qualitatively), some different ideas are to be introduced. In the above discussion it was found that it is  $M_3$  (third moment) which could be responsible for negative values of  $\Delta\nu$ . On this basis one can think of a density distribution function,  $P(\rho_{10c})$ , which is asymmetric particularly for bulk density close to  $\rho_c$ .

At this point then the concept of molecular clusters is introduced, and fluctuations in  $\rho_{10c}$  are considered to be caused by formation of these clusters. In the simplest approach one can make a sharp distinction between two species of molecules, namely, clustered and unclustered, and thereby also differentiate between the local density of unclustered molecules and the internal cluster density. The number and size of the molecular clusters are expected to be very small for low bulk density and an increase is expected with increasing density. Again for simplicity, consider the density

FIGURE 4.9

Suggested model for the density distribution function  $P(\rho_{loc})$  involving unclustered molecules (solid curves) and clustered molecules (dotted curves):

- (a) for bulk density  $\rho_1$ ,
  - (b) for bulk density  $\rho_2 > \rho_1$ ,
  - (c) for bulk density  $\rho_3 > \rho_2$ ,
  - (d) for bulk density  $\rho_4 \sim \rho_{cc}$ ,
- and
- (e) for bulk density  $\rho_5 > \rho_{cc}$ .

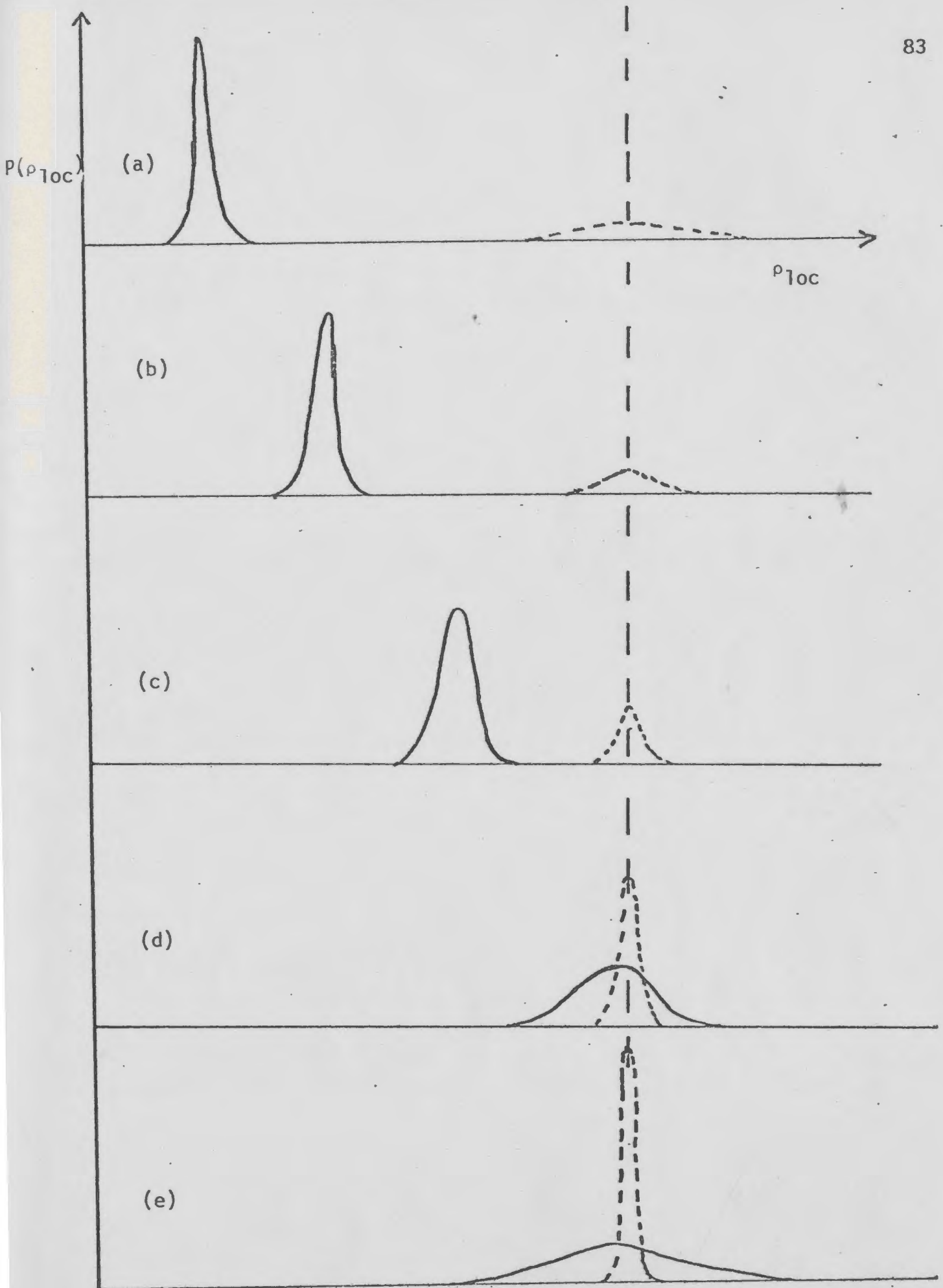


Fig. 4.9

distribution function  $P(\rho_{10c})$  to consist of two separate Gaussian distributions for unclustered molecules and clustered molecules as shown in Fig. (4.9). A suggested evolution of the distribution,  $P(\rho_{10c})$ , with bulk density,  $\rho$ , is also illustrated and, of course, in general the distribution is asymmetric. It is suggested by Clouter et al. (49) that a cluster condensation occurs at a particular bulk density  $\rho_{cc}$  (corresponds to vertical dashes in Fig. (4.9)) which is characterized by a large and sudden change in the mean life time of the clusters ( $\tau_c$ ). As a consequence of the above it is expected that in the region of the anomaly for  $\rho < \rho_{cc}$  the unclustered molecules give rise to the sharp component in the Raman spectrum accompanied by a very broad and weak component due to the clustered molecules, where as for  $\rho > \rho_{cc}$  the sharp component is due to the clustered molecules accompanied by a broad and weak contribution due to unclustered molecules, as shown in Fig. (4.10). Since, the effect of cluster-formation in the region  $\rho < \rho_{cc}$  is to make more room for unclustered molecules and hence to reduce  $\rho_{10c}$  for unclustered molecules, therefore, the relative Raman shift is expected to be less than those obtained using  $\rho$  (bulk density), this can account for positive  $\Delta\nu$ . In the region  $\rho > \rho_{cc}$  the internal cluster density is greater than  $\rho$ , therefore, one expects to observe a relative Raman shift greater in magnitude than obtained using  $\rho$ , thus accounting for negative  $\Delta\nu$ . A sharp change in  $\nu - \nu_0$  can well be attributed to the cluster condensation which reverses the roles of clustered and unclustered molecules. The whole process is pictorially shown in Fig. (4.10). Any increase in density beyond the anomalous region will eventually make the mean internal cluster

FIGURE 4.10

Suggested synthesis of the Raman Q-branch intensity distribution due to unclustered molecules and clustered molecules is shown for densities close to  $\rho_{CC}$ .

(a) Intensity distribution due to unclustered molecules (solid curve) and due to clustered molecules (dotted curve) at bulk density  $\rho < \rho_{CC}$ .

(b) Intensity distribution due to unclustered molecules (solid curve) and due to clustered molecules (dotted curve) at bulk density  $\rho > \rho_{CC}$ .

(c) Indicates how the frequency shifts of the individual components due to unclustered and clustered molecules near  $\rho_{CC}$  can give rise to anomalous behavior in  $(\nu - \nu_0)$  vs.  $\rho$  curve.

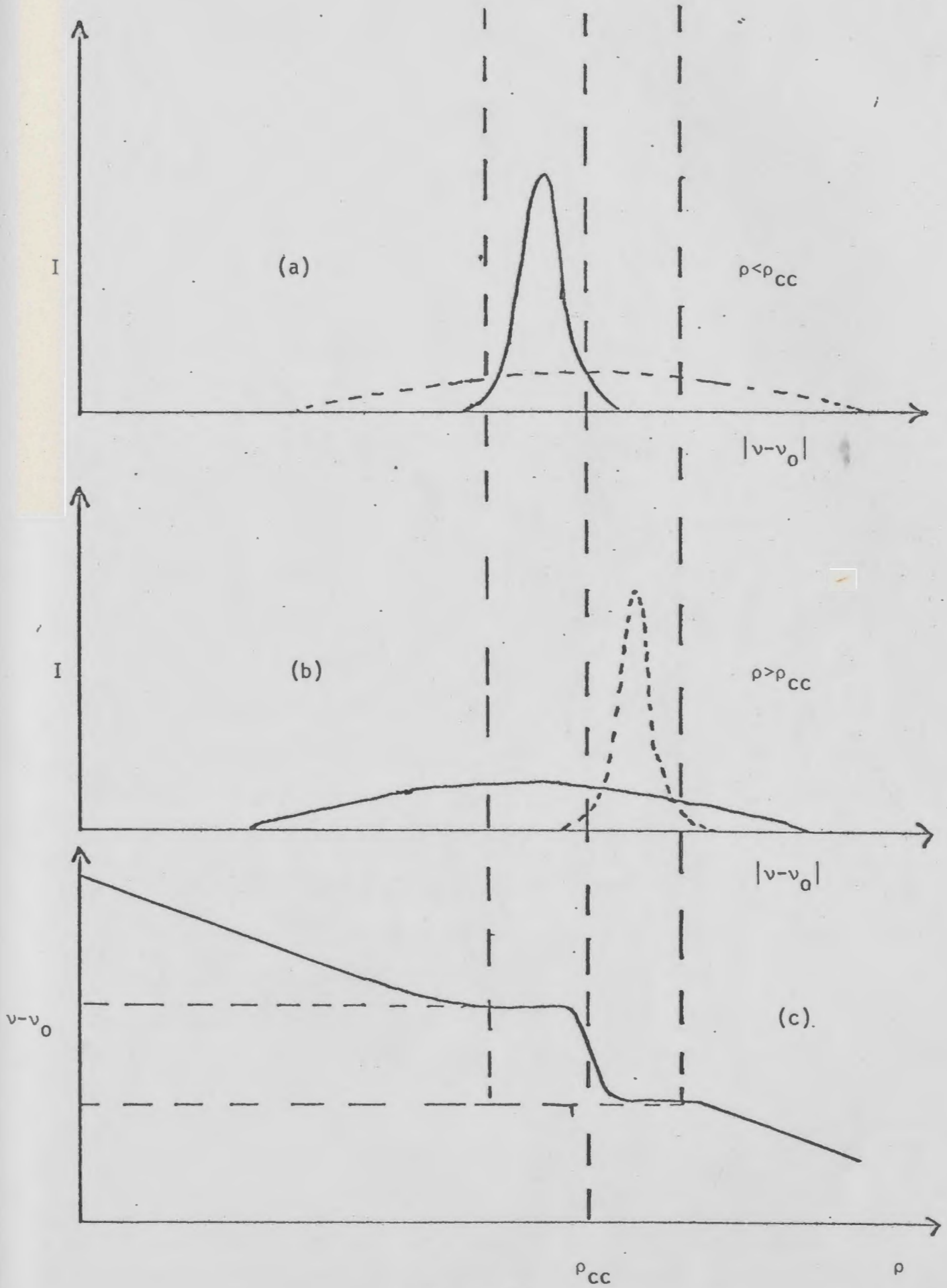


Fig. 4.10

density equal to the bulk density and hence the anomaly will disappear.

Based on the ideas introduced above the anomaly has, in particular, been discussed in more detail for  $O_2$  in the Appendix A. It is noticed that the effect of being farther from  $T_c$  is more on the negative part of  $\Delta v$ , this implies that the number of clusters and their lifetime decreases, in other words, the mean internal cluster density quickly approaches the bulk density, which is evident in the Figs. (4.2-4.4).

In the case of  $N_2$ ,  $\Delta v$  has positive as well as negative values (like in  $O_2$ ) at  $T-T_c = 0.73K$ , and  $T-T_c = 1.80K$ , while it has only positive values at  $T-T_c = 5.73K$  as shown in Fig. (4.2). It is found that in the case of CO there is absence of negative  $\Delta v$  even for  $T-T_c = 0.13K$ . This can perhaps be understood for two reasons, i) the value assumed for  $T_c$  may be greater than the actual value (there is a discrepancy of about  $\pm 0.1K$  in the value of  $T_c$  for CO in the literature and ii) the mean internal cluster density in case of CO quickly becomes equal to the bulk density even for  $T-T_c = 0.13K$ . It is expected that the negative  $\Delta v$  can be found for CO also if  $T_c$  were approached more closely.

To further extend the ideas introduced earlier for a qualitative interpretation a very simple calculation is presented as a first approximation. It is assumed in the most simplified way that  $P(\rho_c)$  is a  $\delta$ -function in each of the ranges,  $\rho < \rho_{cc}$  and  $\rho > \rho_{cc}$ .

A few quantities are defined as follows,

$\tilde{n} \equiv$  internal cluster density, assumed as a constant (approximately),

$c \equiv$  mean number of molecules per cluster,

$\tilde{N}_c \equiv$  mean number of clusters per unit volume  $V$ ,

$N \equiv$  mean number of molecules per unit volume, it is nothing but bulk density.

$\tilde{N}_c/N \equiv n$ , cluster concentration.

Considering the fore-said assumption and equation (4.2), the relative Raman shift  $\nu - \nu_0$  for clustered molecules will have only a first order term, namely,

$$\begin{aligned} (\nu - \nu_0)_c &= a_1 \tilde{n} \\ \text{for } a_1 &= a \\ (\nu - \nu_0)_c &= a \tilde{n} \end{aligned} \quad (4.5)$$

Similarly, for unclustered molecules one can write

$$(\nu - \nu_0)_u = a \frac{(\tilde{N} - c\tilde{N}_c)}{(1 - Ncn/\tilde{n})} \quad (4.6)$$

where,  $(\tilde{N} - c\tilde{N}_c)$  = mean number of unclustered molecules per unit volume,

$(1 - Ncn/\tilde{n})$  = fraction of unit volume available to unclustered molecules

and,  $Ncn/\tilde{n}$  = fraction of unit volume occupied by clusters.

The equation (4.6) can be re-written as

$$(\nu - \nu_0)_u = a \tilde{n} \frac{N(1 - cn)}{(\tilde{n} - Ncn)} \quad (4.7)$$

where,  $cn$  = fraction of molecules in cluster form. Now,  $\Delta\nu$  in the region  $\rho < \rho_{cc}$ , considering the  $\delta$ -function assumption is given by

FIGURE 4.11

Shows the occurrence of the anomaly in  $\Delta v$  vs.  $\rho$ , given by the equations (4.8) & (4.9).  $\Delta v_u$  is contribution due to unclustered molecules and  $\Delta v_c$  is that due to clustered molecules.

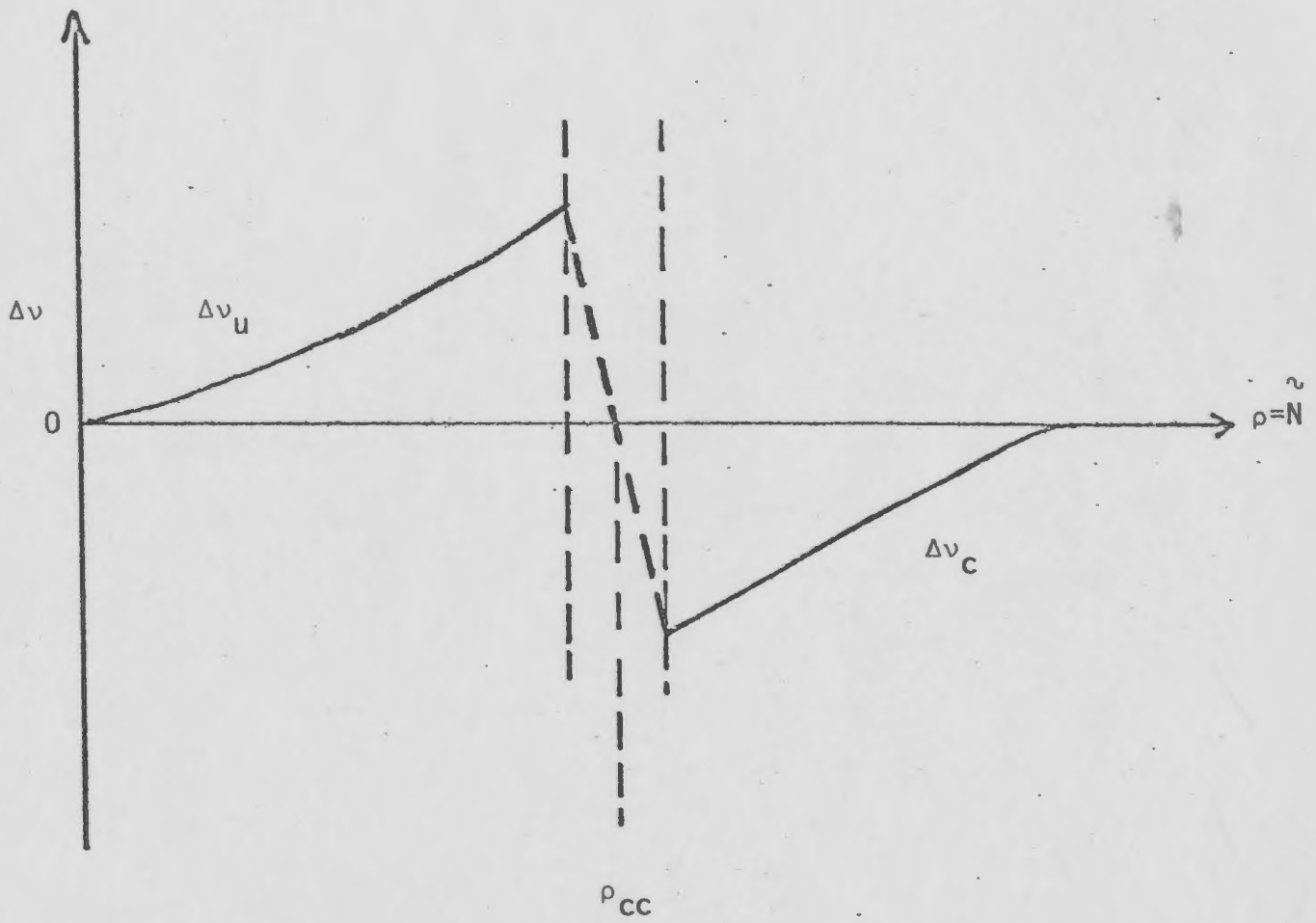


Fig. 4.11

$$\Delta v_u = |a| \tilde{N} \{1 - \tilde{n} (1 - cn)/(\tilde{n} - Ncn)\} \quad (4.8)$$

$$\geq 0$$

where,  $(v-v_0)_N^{\sim} = aN^{\sim}$ . Similarly, in the region  $\rho > \rho_{CC}$ , with the help of equation (4.5),

$$\Delta v = \Delta v_c = (v-v_0)_N^{\sim} - (v-v_0)_c$$

and

$$\Delta v_c = |a| (\tilde{N} - \tilde{n}) \leq 0 \quad (4.9)$$

From the equations (4.8) and (4.9) it is easy to see that a plot of  $\Delta v$  and  $\rho = \tilde{N}$  will look like a curve as shown in Fig. (4.11). It is noted that both the positive as well as negative feature of  $\Delta v$  is evident even after such an over-simplification of the problem by assuming a  $\delta$ -function distribution. This supports the ideas introduced for at least a qualitative interpretation of the anomaly in the relative Raman frequency shift studies.

#### (b) Line-Width (FWHM), $\Gamma$

The full-width at half maximum (FWHM),  $\Gamma(\rho, T-T_c)$ , at temperature  $T$ , of the Raman Q-branches for  $N_2$ ,  $O_2$  &  $CO$  molecules is plotted against density ( $\rho$ ) and reduced density ( $\rho/\rho_c$ ) in Figs. (4.5-4.8). A quantity  $\Delta\Gamma$  is defined as,

$$\Delta\Gamma = \Gamma(\rho, T-T_c) - \Gamma(\rho, T_M-T_c) \quad (4.10)$$

where,  $T$  and  $T_M$  are same as in the case of  $\Delta v$ . Similar to  $\Delta v$ ,  $\Delta\Gamma$  can also have positive as well as negative values. It is noticed from the Figs. (4.5-4.7) that  $\Delta\Gamma$  has negative values only

for  $O_2$  at  $T-T_c = 0.12K$ , while for  $N_2$  and  $CO$  only positive values of  $\Delta\Gamma$  are evident.

It is pointed out in Chapter 2 that the process of motional narrowing is of greatest importance in the present context. Consequently, it is expected from the theory of motional narrowing (23-25), discussed in Chapter 2, that the Raman Q-branch line-width should vary approximately as  $\rho^{-1}$  in the density range where the band is symmetrical ( $\rho > 150$  Amagat in this experiment). The anomalous behavior exhibited in the Figs. (4.5-4.7) is in contradiction to the behavior expected for the motional narrowing phenomenon. This anomaly in width can also be interpreted (at least qualitatively) in terms of the ideas of 'local density' and 'cluster formation', already introduced in the previous section.

Similar to the case of  $\Delta\nu$ , it is the local density of the unclustered molecules which is perhaps responsible for the Raman line-width in the positive  $\Delta\Gamma$  region. For  $\rho < \rho_{cc}$ , the presence of clusters tends to decrease the local density of unclustered molecules, as mentioned in the previous section. As a consequence, the Raman line-width (because of the  $\rho^{-1}$  dependence) will be greater than expected due to the bulk density. Increasing the bulk density (in the region  $\rho < \rho_{cc}$ ) may further increase the cluster concentration with negligible effect on the cluster life time  $\tau_c$ , and this leads to a further decrease in the local density of unclustered molecules, and hence a further increase in the line-width. This accounts for the positive values of  $\Delta\Gamma$ , at the same time it is evident from the Figs. (4.5-4.7) that the width  $\Gamma(\rho, T-T_c)$  is relatively greater

(in region close to  $\rho_{CC}$ ) than the extrapolated value at  $\rho = 0$ , (i.e.,  $\Gamma(0, T-T_C)$ ). This is not explainable in terms of the motional narrowing phenomenon.

To account for this behavior it is proposed by Clouter et al. (49) that the life time effects of unclustered molecules should be introduced. A quantity  $\tau_u$  is defined as the average life time of the unclustered molecules. If  $\tau_c$  is the 'cluster life time' than one can assume that:

$$\tau_u = (1/nc - 1) \tau_c \quad (4.11)$$

where,  $nc$  is the fraction of molecules in cluster form. The contribution to the line-width due to  $\tau_u$  will be of the form,

$$\Gamma_u \propto \{(1/nc - 1) \tau_c\}^{-1} \quad (4.12)$$

where,  $\Gamma_u$  is defined as the line-width due to  $\tau_u$ . If the line-width due to motional narrowing phenomenon determined by local density of unclustered molecules is denoted by  $\Gamma_{MN}^u$ , then the total line-width in region  $\rho < \rho_{CC}$  can be approximated by,

$$\Gamma = \Gamma_{MN}^u + \Gamma_u \quad (4.13)$$

If it is assumed, as mentioned above, that an increase in the bulk density in region  $\rho < \rho_{CC}$  has the effect of an increase in cluster concentration (with negligible effect on  $\tau_c$ ) then it has a two-fold effect on the line-width. Firstly, a decrease in  $\rho_{loc}$  of unclustered molecules leads to an increase in the line-width as discussed earlier; secondly an increase in the cluster concentration

leads to a decrease in  $\tau_u$  (eqn. (4.11)), which in turn leads to a further increase in the Raman line-width (see eqn. (4.12)). This accounts for the Raman line-width being greater than the extrapolated value at  $\rho = 0$ .

It has already been suggested that, at  $\rho_{CC}$  the role of unclustered molecules is reversed by that of the clustered molecules and there is a sudden large change in the cluster life time leading to cluster condensation. This is consistent with the sharp decrease in line-width at  $\rho_{CC}$ .

In the region  $\rho > \rho_{CC}$ , the Raman line-width consists of two contributions namely, i)  $\Gamma_{MN}^C$ , the motional narrowing contribution due to the mean internal cluster density and ii)  $\Gamma_C$ , the cluster life time contribution. Therefore, the total width in the region  $\rho > \rho_{CC}$  can again be approximated by:

$$\Gamma = \Gamma_{MN}^C + \Gamma_C \quad (4.14)$$

Since, the mean internal cluster density is greater than the bulk density,  $\Gamma_{MN}^C$  will be less than the width due to the bulk density (determined by motional narrowing),  $\Gamma_{MN}^P$ . To have a negative value of  $\Delta\Gamma$ , as observed for  $O_2$  at  $T - T_C = 0.12K$  (Fig. (4.6)). The condition  $(\Gamma_{MN}^C + \Gamma_C) < \Gamma_{MN}^P$  is necessary. It is expected that in the case of  $O_2$  for  $T - T_C = 0.12K$ , the cluster life time  $\tau_C$  is large enough near  $\rho_{CC}$  (in region  $\rho > \rho_{CC}$ ) so as to contribute very little to  $\Gamma_C$ . This in turn may lead to the condition  $(\Gamma_{MN}^C + \Gamma_C) < \Gamma_{MN}^P$ , giving rise to the observed negative value of  $\Delta\Gamma$  for  $O_2$ . There are no negative values of  $\Delta\Gamma$  observed at  $T - T_C = 0.95K$  or higher for  $O_2$  or for any temperature in the case of  $N_2$  and  $CO$ .

This would mean that the condition  $(\Gamma_{MN}^C + \Gamma_C) \approx \Gamma_{MN}^0$  is probably fulfilled. If in  $O_2$  (at  $T-T_c = 0.12K$ ),  $N_2$  (at  $T-T_c = 0.73K$ ) and  $CO$  (at  $T-T_c = 0.13K$ ) it is assumed that for densities very close to  $\rho_{cc}$  ( $\rho > \rho_{cc}$ ) the cluster life time  $\tau_c$  is small enough to contribute significantly to the width  $\Gamma_C$  then the condition  $(\Gamma_{MN}^C + \Gamma_C) \approx \Gamma_{MN}^0$  may be full filled leading to the observed results.

An interesting feature of the data presented in Figs. (4.5-4.7) is the persistence of a broad maximum even for the highest temperatures where no critical effects are evident. This is in contradiction to what is expected on the basis of motional narrowing theory ( $\rho^{-1}$  dependence) for higher densities. This effect could be attributed to the presence of Van der Waal's molecules, which are expected to exist even at such high temperatures (49). If it is assumed that the concentration of such molecules is determined mainly by temperature while their life times by density, then the observation of the broad maximum in the Raman line-widths, with no such effect in relative Raman shift data, can be understood easily. As for the above assumption it is the life time of Van der Waal's molecules which is mainly responsible for the broad maxima at a certain temperature.

REFERENCES

1. G. Placzek, Handbuch der Radiologie, Marx, E. (ed.), Leipzig 6(2), 209-374 (1934) (English Translation in UCRL Trans. No. 526 (L)).
2. G. Herzberg, Mol. Spectra and Mol. Structure, D. Van Nostrand Company, New York, (1950).
3. J. Fiutak & J. Van Kranendonk, Can. J. Phys., 41, 21 (1963).
4. J. Fiutak & J. Van Kranendonk, Can. J. Phys., 40, 1085 (1962).
5. J. Van Kranendonk, Can. J. Phys., 41, 433 (1963).
6. C. G. Gray & J. VanKranendonk, Can. J. Phys., 44, 2411 (1966).
7. R. G. Gordon, J. Chem. Phys., 44, 3083 (1965).
8. R. G. Gordon, J. Chem. Phys., 45, 1649 (1966).
9. A. D. May, V. Degen, J. C. Stryland and H. L. Welsh, Can. J. Phys., 39, 1769 (1961).
10. A. D. May, G. Varghese, J. C. Stryland and H. L. Welsh, Can. J. Phys., 42, 1058 (1964).
11. S. S. Bhatnagar, E. J. Allin and H. L. Welsh, Can. J. Phys., 40, 9 (1962).
12. G. Varghese, Ph.D. Thesis, Univ. of Toronto, Canada (1967).
13. W. R. L. Clements, Ph.D. Thesis, Univ. of Toronto, Canada (1972).
14. P. Dion and A. D. May, Can. J. Phys., 51, 36 (1973).
15. P. Dion, M. Sc. Thesis, Univ. of Toronto, Canada (1972).
16. T. Witkowitz and A. D. May, Can. J. Phys., 54, 575 (1976).
17. T. Witkowitz, M. Sc. Thesis, Univ. of Toronto, Canada (1975).
18. N. Bloembergen, E. M. Purcell and R. V. Pound, Phys. Rev; 73, 679 (1948).
19. A. D. May, Ph.D. Thesis, Univ. of Toronto, Canada (1959).
20. E. Allin, A. D. May, B. Stoicheff, J. Stryland, and H. L. Welsh, Appl. Opt., 6, 1597 (1967).

21. M. Scotto, J. Chem. Phys., 49, 5362 (1968).
22. W. R. L. Clements and B. P. Stoicheff, Appl. Phys. Letts., 12, 246 (1968).
23. V. Alekseyev and I. I. Sobelman, Sov. Phys. JETP, 28, 991 (1969).
24. V. Alekseyev, A. Grasiuk, V. Ragulsky, I. I. Sobelman and F. Faizulov, IEEE J. Quantum, Elect., 4, 654 (1968).
25. S. I. Temkin and A. I. Burshtein, JETP Lett., 24, 2 (1976).
26. S. R. J. Brueck, Chem. Phys. Letts; 50, 516 (1977).
27. A. D. May, J. C. Stryland and G. Varghese, Can. J. Phys., 48, 2331 (1970).
28. C. H. Wang and R. B. Wright, J. Chem. Phys., 59, 1706 (1973).
29. Y. LeDuff, J. Chem. Phys., 59, 1984 (1973).
30. Y. LeDuff and W. Holzer, Chem. Phys. Letts., 24, 212 (1974).
31. K. Altmann, W. Holzer and Y. LeDuff, Chem Phys. Letts., 36 259 (1975).
32. M. J. Clouter and H. Kiefte, J. Chem. Phys., 66, 1736 (1977).
33. M. J. Clouter, H. Kiefte and N. Ali, to be published.
34. D. Von der linde, A. Laubereau and W. Kaiser, Phys. Rev. Lett., 26, 954 (1971).
35. A. Laubereau, Chem. Phys..Letts., 27, 600 (1974).
36. S. F. Fischer and A. Laubereau, Chem. Phys. Letts., 35, 6 (1975).
37. L. Mannik and J. C. Stryland, Can. J. Phys., 50, 1355 (1972).
38. C. G. Gray and H. L. Welsh, in Essays in Structural chemistry (MacMillan, London, 1971).
39. A. D. May and J. D. Poll, Can. J. Phys., 43, 1836 (1965).
40. T. Kihara, Advances in Chemical Physics, (Interscience, New York), Vol. 1, (1958).

41. I. E. Morgan, M. Sc. Thesis, Memorial Univ. Canada (1976).
42. M. J. Clouter, H. Kiefte and I. E. Morgan, *Can. J. Phys.*, 53, 1727 (1975).
43. J. Bonamy, L. Bonamy and D. Robert, *J. Chem. Phys.*, 67, 4441 (1977).
44. J. O. Hirschfelder, C. F. Curtiss and R. B. Bird, *Molecular Theory of Gases and Liquids*, (John Wiley & Sons, Inc (1954)). The Lennard-Jones  $\sigma$ , for  $N_2$ ,  $O_2$  and CO are approximately, 0.36 nm, <sup>2</sup>0.35 nm, and 0.36 nm respectively.
45. R. D. McCarty and L. A. Weber, *Natl. Bur. Stand. Tech. Note* 384 (July 1971).
46. R. T. Jacobsen and R. B. Stewart, *J. Phys. Chem Ref. Data*, 2, 4, 757 (1973).
47. J. G. Hust and R. B. Stewart, *Natl. Bur. Stand. Tech. Note* 202 (Nov. 1963).
48. H. W. Leidecker, Jr., and J. T. LaMacchia, *J. Acoust. Soc. Am.*, 43 143 (1968).
49. M. J. Clouter, H. Kiefte and N. Ali, *Phys. Rev. Letts*; 40 1170 (1978).

PREVIOUSLY COPYRIGHTED MATERIAL,  
IN APPENDIX A, LEAVES 99-102,  
NOT MICROFILMED

ANOMALOUS BEHAVIOR IN THE VIBRATIONAL RAMAN SPECTRUM OF OXYGEN  
UNDER NEAR-CRITICAL CONDITIONS.

M.J. CLOUTER, H. KIEFTE, AND N. ALI

DEPARTMENT OF PHYSICS, MEMORIAL UNIVERSITY OF NEWFOUNDLAND, ST. JOHN'S. NEWFOUNDLAND A1B 3X7

COPYRIGHT 1978 The American Physical Society  
Leaves 1170-1173

## APPENDIX A

## Anomalous Behavior in the Vibrational Raman Spectrum of Oxygen under Near-Critical Conditions

M. J. Clouter, H. Kieft, and N. Ali

*Department of Physics, Memorial University of Newfoundland, St. John's, Newfoundland A1B 3X7, Canada*

(Received 24 February 1978)

The isothermal density dependence of both the shift and width of the Raman Q branch in oxygen gas have been found to exhibit anomalous behavior under near-critical conditions. The observed effects are interpretable in terms of molecular-cluster formation, and it is concluded that the Raman effect is a potentially valuable probe of density fluctuations in the critical region.

The density-dependent effects of intermolecular forces upon the vibrational Raman spectra of gases have been the subject of extensive experimental and theoretical work.<sup>1</sup> As a result, these effects are now fairly well understood for values of reduced temperature ( $T/T_c$ ) greater than about 2. In the present context the essential points are (i) that at low densities the resolved structure of the pure vibrational Raman spectrum is characterized by frequency shifts which are predominantly linear in the density,<sup>2</sup> and (ii) that at sufficiently high densities this polarized Q branch is subject to a narrowing process where the width varies as the inverse of the density.<sup>3</sup> In this Letter we present new experimental results for O<sub>2</sub> gas in the neighborhood of its critical point where the influence of density fluctuations may be responsible for departures in the behavior of the polarized spectrum from that expected on the basis of previous work. As a consequence we sug-

gest that such experiments are capable of providing significant information regarding the nature of these fluctuations.

The data, which are presented graphically in Fig. 1, were obtained using previously described interferometric techniques.<sup>4</sup> The experimental errors in the determination of the relative frequency shift and the width are estimated to be  $\pm 2\%$  and  $\pm 7\%$ , respectively. Gas densities were determined using published PVT data,<sup>5</sup> the absolute temperature and pressure being measured within limits of  $\pm 0.02$  K and  $\pm 0.07$  bar, respectively. It is recognized that the resulting uncertainty in the density may be considerable in the neighborhood of the critical density<sup>6</sup> (304 amagat). However, in this preliminary report we wish to emphasize the qualitative features of the observations, it being considered highly improbable that experimental errors could account for the anomalous, and quite reproducible, behavior which oc-

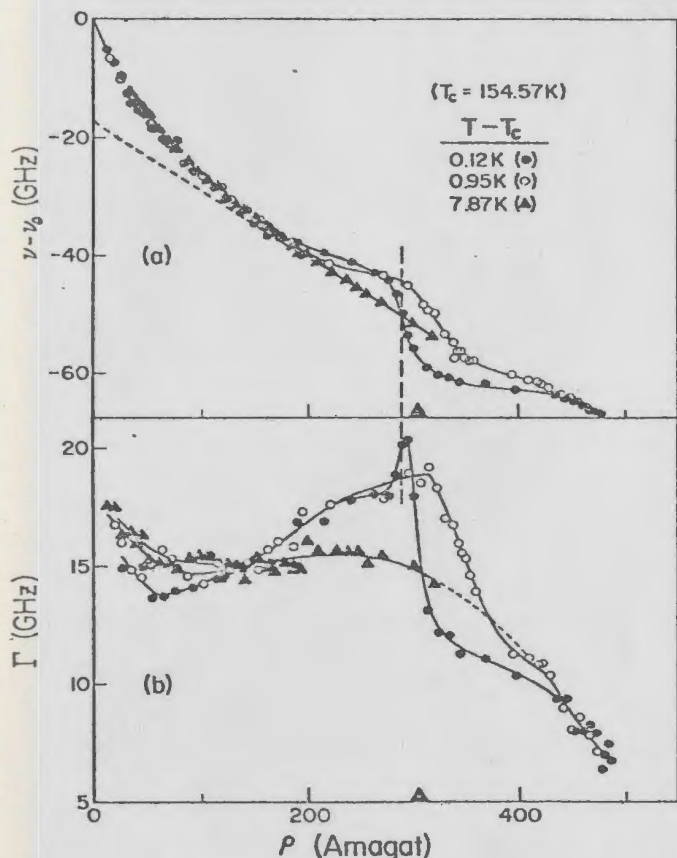


FIG. 1. High-resolution data showing the behavior of the Raman Q branch of  $O_2$  gas in the critical region ( $\rho_c = 304$  amagat). (a) The peak frequency shift relative to the value at zero density ( $\nu_0$ ), as a function of density; (b) the full width at half-maximum, as function of density. Measurements were made using a scanning Fabry-Perot interferometer with a spectral free range of 110.7 GHz and a finesse of  $\sim 70$ . The maximum attainable density for  $T - T_c = 7.87$  K was determined by the pressure limitations of the sample cell. See text for discussion of the linear extrapolation to  $\rho = 0$  in (a).

curs for  $T - T_c < 2$  K. This comment is directed in particular at the occurrence of a sharp maximum in the linewidth data of Fig. 1(b); such a phenomenon is not amenable to explanation in terms of possible gravity-induced density gradients, for example. In addition, we point out that considerable care was taken to ensure, insofar as possible, that equilibrium conditions were established for each measurement. Each pair of data points in Fig. 1 represents an average initial waiting period of  $\sim 1$  h followed by a spectrum accumulation time of  $\sim 2$  h.

The vibrational Raman frequencies,  $\nu(\rho, T - T_c)$ , are plotted relative to the value for  $\rho = 0$  (which was obtained by extrapolation), the temperature dependence of the latter quantity being negligible

over the  $\sim 8$ -K range so that  $\nu(0, T - T_c) \equiv \nu_0$ . As discussed below, the nonlinear behavior of the data at low densities ( $\rho < 150$ ) is to be expected on the basis of known effects already treated in the literature; it is the nonlinear, dispersionlike behavior in the region  $150 < \rho < 440$  which is of primary interest here. Figure 1(a) demonstrates the essential characteristics of this phenomenon; in particular, it is only readily observable for  $T - T_c < 1$  K. A similar comment also applies to the linewidth data of Fig. 1(b): The broad maximum which occurs in the region  $150 < \rho < 440$  for  $T - T_c > 1$  K quite abruptly develops into a very sharp maximum for  $T - T_c < 1$  K. The correlation between the behavior of the shift and width is also apparent, and a vertical dashed line has been drawn in Fig. 1 to emphasize this point for the case of  $T - T_c = 0.12$  K.

Additional data not shown in Fig. 1 include a corresponding series of intensity measurements; and, in this connection, we emphasize an important characteristic of Fabry-Perot spectrometry as employed in these experiments: A spectral contribution whose width is greater by about an order of magnitude than the component being examined will occur only as a background level regarding which very little information can be extracted.<sup>4</sup> However, since the Q-branch scattering is highly polarized, it was readily verified that a substantial contribution to the Q-branch intensity was contained within the above-mentioned background. These measurements were performed under conditions of lowest practical resolution<sup>7</sup> with the scattered light restricted by filtering to a bandwidth of  $\sim 5000$  GHz, centered at  $\nu_0$ . It is consequently concluded that the complete spectrum of the polarized Raman scattering includes not only the sharp component to which the data of Fig. 1 apply, but also a contribution whose width is greater by at least an order of magnitude. The intensity of the polarized background relative to that at the peak of the sharp component at  $T - T_c = 0.12$  K was found to exhibit a distinct minimum in the same narrow density range where the corresponding width of Fig. 1(b) reached a maximum, i.e., for  $\rho \approx 290$ .

Published data<sup>2</sup> for  $H_2$  at 85 K, for example, show that the vibrational Raman shifts are proportional to density in the region  $\rho < 300$  where the individual Q-branch components (of  $H_2$ ) are well resolved. In the present case of  $O_2$  the (zero-density) Q-branch structure is unresolvable and the departure from linear behavior for  $\rho < 150$  is to be expected on the basis of current theories<sup>3,8</sup>

of the particular *motional-narrowing* phenomenon which becomes important when the frequency of rotationally inelastic collisions is comparable (in appropriate units) to the vibration-rotation interaction energy. The narrowing which occurs with increasing density is accompanied by a change in the shape of the band from its characteristic asymmetrical form at very low densities<sup>9</sup> to a highly symmetrical form for  $\rho > 150$ . The shift in the peak frequency which is associated with the latter process is also responsible for the non-linear behavior of  $\nu - \nu_0$  in the region  $\rho < 150$ . It is to be noted that the shift data for  $T - T_c = 7.87$  K exhibit the anticipated linear dependence on density for  $\rho > 150$  and, as a matter of interest, Fig. 1(a) includes a linear extrapolation to zero density which, we feel, represents the direct effects of intermolecular interaction upon the  $O_2$  vibrational frequency when critical effects are negligible.

Any interpretation of the previously described anomalous behavior must recognize the essential short-range nature of the intermolecular interactions involved. The range parameter is, in fact, of order 1 nm,<sup>10</sup> so that the density to which a single Raman-scattering event is sensitive should most appropriately be identified as a "local density,"  $\rho_{loc}$ , corresponding to a volume element of  $\sim 1 \text{ nm}^3$ , rather than the bulk density,  $\rho$ . Consequently, under near-critical conditions, one can sensibly expect that fluctuations in  $\rho_{loc}$  will play a key role in accounting for the observed behavior of the Raman spectrum.

In the following discussion, attention is focused on the observations for  $T - T_c = 0.12$  K and, for convenience, we define the quantities  $\Delta\nu = \nu(\rho, 0.12) - \nu(\rho, 7.87)$  and  $\Delta\Gamma = \Gamma(\rho, 0.12) - \Gamma(\rho, 7.87)$ , which have positive and negative values throughout approximately the same density ranges, namely,  $150 < \rho < 300$  and  $300 < \rho < 440$ , respectively. We associate fluctuations in  $\rho_{loc}$  with the formation of molecular clusters, and suggest that a *cluster condensation* occurs near the critical density,  $\rho_c$ . The basis of our interpretation is the assumption that this cluster condensation can be characterized in part by a large and sudden change in the mean cluster lifetime,  $\tau$ . As a consequence, the sharp component which is observed in the high-resolution Raman spectrum behaves as a selective detector of (i) unclustered molecules in the  $\Delta\nu > 0$  region and (ii) clustered molecules in the  $\Delta\nu < 0$  region. This proposal and the ensuing ideas are, we feel, substantiated in an important way by the intensity measurements previously

described.

At the low-density extreme of the  $\Delta\nu > 0$  region, one can argue (i) that the fraction  $n$ , of  $O_2$  molecules which occur in cluster form, as well as the size of any such clusters, will be small, and (ii) that  $\tau$  may be comparable to the mean collision time. Under these conditions, any Raman scattering from clustered molecules will be weak and conceivably recognizable only as a background contribution to the high-resolution spectrum because of its large, lifetime-limited width. The sharp spectral component which is observed in this region can thus be associated with unclustered molecules, and the principal (observable) effect of cluster formation will be the indirect one of giving rise to a *decrease* in the local density of these unclustered molecules. This, in turn, will give rise to observed relative Raman shifts which are lower in magnitude than those expected from a linear dependence on bulk density. If a small increase in  $\rho$  is now associated primarily with an increase in  $n$ , there being no great change in  $\tau$ , the effect upon the shift will be enhanced so that the quantity,  $\Delta\nu$ , can be expected to increase in magnitude with a positive sign, as observed. As implied above, the cluster condensation may be regarded as reversing the roles of clustered and unclustered molecules due to a sharp increase in  $\tau$ ; that is, for  $\rho > \rho_c$ ,  $n$  may approach unity and most of the molecules are presumed to occur in the form of relatively long-lived clusters of large size. The Raman scattering from unclustered molecules then becomes very broad and weak so that the observed component becomes, in effect, a probe of the internal cluster densities which, being higher than the bulk density, can account for the negative values of  $\Delta\nu$ . As the bulk density is further increased it will eventually approach the mean internal-cluster density at which point the effect should disappear, again in accordance with observations for  $\rho \approx 440$ .

It has been demonstrated<sup>4,8,11</sup> that vibrational dephasing processes represent the most important contribution to the linewidth at the highest densities in the saturated liquid. In the present case, however, it is most probable that, of the processes which have been discussed in the literature, it is the motional-narrowing mechanism which is of greatest importance. Consequently, the width can be expected<sup>3</sup> to vary approximately as  $\rho^{-1}$  when the density is sufficiently high so that the Q-branch profile is symmetrical, i.e., for  $\rho > 150$  in the case of  $O_2$ . This behavior is obviously not reflected in the data of Fig. 1(b), but

ideas already introduced are consistent with the observed behavior.

Given that in the  $\Delta\Gamma > 0$  region it is the local density of unclustered molecules which should determine the width of the observed Raman line, then, because of its inverse density dependence, the linewidth should indeed be greater than expected on the basis of a bulk density calculation. However, this effect cannot account for the fact that  $\Gamma$  exceeds its (extrapolated) zero-density value over a considerable part of this region, so that some additional contribution is apparently involved. In this connection, one can naively define a quantity  $\tau'$  representing the average time during which a typical  $O_2$  molecule is *not* part of a cluster. The equilibrium requirement,  $n/(1-n) = \tau'/\tau$ , then leads to  $\tau' = (n^{-1} - 1)\tau$ , whence it is apparent that  $\tau'$  can be expected to *decrease* with increasing  $\rho$  in this region provided, *and as previously assumed*, that  $n$  increases substantially with  $\rho$  while there is no great change in  $\tau$ . Such a decrease in  $\tau'$  may consequently account for the additional contribution to  $\Gamma$ .

The sharp decrease in linewidth which occurs near  $\rho_c$  is clearly consistent with the presumed nature of the cluster condensation as already outlined. In addition, the existence of a  $\Delta\Gamma < 0$  region is to be expected if the linewidth in this region is not limited by cluster-lifetime considerations. Such being the case,  $\Gamma$  could be determined primarily by the (mean, internal) cluster density via the motional-narrowing process; i.e., the associated inverse density dependence together with a mean local density which is higher than the bulk value could give rise to negative values of  $\Delta\Gamma$ .

An additional interesting feature of the linewidth data of Fig. 1(b) is that an approximate  $\rho^{-1}$  dependence is not apparent even at temperatures as high as  $T - T_c = 7.87$  K, whereas  $\nu(\rho)$  reverts to the expected linear behavior for  $T - T_c > 2$  K. It seems reasonable to attribute the persistence of a broad maximum in  $\Gamma(\rho)$  to the presence of small, residual clusters in the form of van der Waals molecules, which indeed can be expected to exist at even higher temperatures. If it is assumed that the fractional concentration of these van der Waals molecules is determined by temperature rather than density, while the converse is true of their mean lifetime, then their manifestation via  $\Gamma(\rho)$  is understandable within the framework of the ideas already advanced. It would therefore appear that it is the distinction between the processes of small- and large-clus-

ter formation which is of essential importance here.

It should be emphasized that the segregation of molecules into two distinct species, namely, clustered molecules and other molecules, represents but an initial attempt to account for the gross features of the anomaly. It is hoped that a better understanding of the anomaly will result from experiments which are now in progress to examine more carefully the broad-band character of the polarized scattering using a grating spectrometer. These results, together with corresponding high-resolution data for  $N_2$  and  $CO$ , will be presented in a more comprehensive publication to appear in the near future.

The experiments described here were undertaken following discussions with Professor H. L. Welsh, Department of Physics, University of Toronto, whose prior work with C. L. Jolliffe had demonstrated unusual behavior in the frequencies of ( $\nu_1, 2\nu_2^0$ ) Raman doublet of  $CO_2$  under near-critical conditions. The authors are indebted to Professor Welsh for communication of these unpublished results and for continuing consultations.

Valuable discussions with Dr. J. C. Lewis, as well as helpful comments from Dr. R. C. Desai, Dr. J. Van Kranendonk, and Dr. A. R. W. McKellar, are also acknowledged. This research was supported by grants from the National Research Council of Canada.

<sup>1</sup>C. G. Gray and H. L. Welsh, *Essays in Structural Chemistry* (MacMillan, London, 1971), and references therein.

<sup>2</sup>A. D. May, G. Varghese, J. C. Stryland, and H. L. Welsh, *Can. J. Phys.* **42**, 1058 (1964).

<sup>3</sup>S. I. Temkin and A. I. Burshtein, *Pis'ma Zh. Eksp. Teor. Fiz.* **24**, 99 (1976) [*JETP Lett.* **24**, 86 (1976)].

<sup>4</sup>M. J. Clouter and H. Kiefte, *J. Chem. Phys.* **66**, 1736 (1977).

<sup>5</sup>R. D. McCarty and L. A. Weber, *Thermophysical Properties of Oxygen from the Freezing Liquid Line to 600 R for Pressures to 5000 Psia*, U. S. National Bureau of Standards, Technical Note No. 384 (U. S. GPO, Washington, D. C., 1971).

<sup>6</sup>Densities will be quoted in amagat units  $\equiv \rho/\rho_{S1P}$  throughout the remainder of this paper.

<sup>7</sup>The spectral free range was approximately 300 GHz ( $10 \text{ cm}^{-1}$ ).

<sup>8</sup>S. R. J. Brueck, to be published.

<sup>9</sup>N. H. Rich and D. W. Lepard, *J. Mol. Spectrosc.* **33**, 549 (1971).

<sup>10</sup>The Lennard-Jones  $\sigma$  for  $O_2$  has a value of approximately 0.35 nm.

<sup>11</sup>A. Laubereau, *Chem. Phys. Lett.* **27**, 600 (1974).





